Research Square

Preprints are preliminary reports that have not undergone peer review.
They should not be considered conclusive, used to inform clinical practice,
or referenced by the media as validated information.

Corn-Stalk-Derived Porous Carbon Coupled Spinel NiCo 2 O 4 Hierarchical Microspheres as Advanced Electrodes for Aqueous Asymmetric Supercapacitors

Yi Chen
Harbin University of Commerce
Mingzhao Xing
Harbin University of Commerce
Haoqi Geng
Harbin University of Commerce
Zhanqiang Wang
Harbin University of Commerce
Hui Zhi
zhih@hrbcu.edu.cn

Harbin University of Commerce

Research Article

Keywords: supercapacitor, nickel cobalt oxide spinel, biomass carbon, pseudocapacitive kinetics, asymmetric device, microgrid

Posted Date: November 24th, 2026

DOI: https://doi.org/10.21203/rs.3.rs-11664658/v1

License: This work is licensed under a Creative Commons Attribution 4.0 International License.
Read Full License

Additional Declarations: No competing interests reported.

Corn-Stalk-Derived Porous Carbon Coupled Spinel $NiCo_2O_4$ Hierarchical Microspheres as Advanced Electrodes for Aqueous Asymmetric Supercapacitors

Yi Chen, Mingzhao Xing, Haoqi Geng, Zhanqiang Wang, Hui Zhi*

School of Light Industry, Harbin University of Commerce, Harbin, China

*Corresponding author: zhih@hrbcu.edu.cn

Abstract

Spinel $NiCo_2O_4$ combines the Ni^{2+}/Ni^{3+} and Co^{2+}/Co^{3+} redox couples and is a leading pseudocapacitive candidate for supercapacitor positive electrodes, but its poor intrinsic conductivity and the restacking of microsphere-assembled nanosheets limit rate capability and long cycling. We follow a chain of screening experiments, structural analysis, kinetic analysis and device validation. $NiCo_2O_4$ microspheres were prepared by a solvothermal-calcination route and porous carbon (BC, BET surface area 327.6 m^2 g^{-1}) was derived from corn stalk by KOH activation; composite electrodes were made by physical blending, and two screening experiments covered hydrothermal temperature (120–180 °C) and oxide:carbon mass ratio (1:9–9:1). Structures were resolved by XRD, XPS, SEM/TEM and BET; CV, GCD and EIS measurements were performed in a three-electrode cell in 2 M KOH, and charge-storage mechanisms were quantified with the power-law model and the surface-capacitive contribution separation. Experiments and analysis jointly show that 160 °C and the 7:3 ratio give the best overall performance; BC preserves the spinel phase and the mixed Ni and Co oxidation states while forming conductive bridges between microspheres and preserving a 1.4/3.6/8 nm hierarchical pore set; the 7:3 electrode delivers 1136 F g^{-1} at 1 A g^{-1}, about 82% above the pure phase, with 79.4% retention at 5 A g^{-1}; a power-law exponent b of 0.71, a 75.4% surface-capacitive contribution at 50 mV s^{-1}, a charge-transfer resistance reduced from about 140 to about 30 Ω, and 87.7% retention after 3000 cycles at 2 A g^{-1}. The commercial activated-carbon anode delivers 165 F g^{-1} at 1 A g^{-1}, with 94.6% retention after 3000 cycles. An asymmetric device (m^+:m^- = 1:2.3) with a commercial activated-carbon negative electrode operates over 0–1.4 V; its cell capacitance is 47.7 F g^{-1} on the total active mass (157.3 F g^{-1} referred to the positive electrode), corresponding to 13.0 Wh kg^{-1} at 212 W kg^{-1} and 8.6 Wh kg^{-1} at 2.1 kW kg^{-1}. The cell retains 89.4% after 10 000 cycles. With a raw-material cost about 36% of graphene-based counterparts, the device offers a low-cost, reproducible power-buffering unit for microgrid frequency-regulation scenarios.

Keywords: supercapacitor; nickel cobalt oxide spinel; biomass carbon; pseudocapacitive kinetics; asymmetric device; microgrid

1 Introduction

In renewable-energy integration and microgrid scenarios, the storage layer performs power smoothing, power-quality regulation and short-time energy shifting. The power-type duty cycle here means bidirectional throughput on a seconds-to-minutes basis, several hundred equivalent cycles per day, which batteries cannot sustain economically [1–3]. Electrochemical supercapacitors sit at the power end of the Ragone plot: electric double-layer capacitors (EDLCs) store charge by ion adsorption at the electrode/electrolyte interface, charging and discharging within tens of seconds over tens of thousands to hundreds of thousands of cycles [4–6]. Consequently, where supercapacitors serve as the power-buffering unit, the energy density and stability of the electrode material set the usable energy and the lifetime economics at device level. This paper therefore concentrates on electrode materials and device mechanisms, and treats the microgrid strictly as application background.

Mechanistically, charge storage in alkaline $NiCo_2O_4$ is commonly written as two reversible Faradaic couples: $NiCo_2O_4 + OH^- + H_2O \leftrightarrow 2NiOOH + Co_2O_3 + e^-$ and $Co_2O_3 + OH^- + H_2O \leftrightarrow 2CoOOH + e^-$, with $CoOOH + H_2O + e^- \leftrightarrow Co(OH)_2 + OH^-$ completing the reduction branch [7–9]. The narrow potential separation of these surface/near-surface redox pairs produces a single broad, overlapping CV peak pair, and caps the positive-electrode window at the oxygen-evolution boundary. Asymmetric devices exploit precisely this asymmetry: pairing a wide-window carbon anion-storage negative electrode with the more positive redox couple of the oxide positive electrode stitches the two stable potential ranges end to end, pushing the cell window from ~0.6 V for a single electrode to above 1.4 V without exceeding water splitting [4,6,10]. Since device energy scales as $E = 0.5 \cdot C \cdot \Delta V^2/3.6$, each additional 0.2 V of stable window raises device energy by roughly one third, which is why window design and charge balancing matter as much as materials chemistry [11].

Regarding the state of the art, reported $NiCo_2O_4$ electrodes converge on a common trade-off: in an annealing-temperature series the 350 °C product delivered 1254 F g^{-1} at 1 A g^{-1} yet retained only 63% after 5000 cycles at 7 A g^{-1}, while the 250 °C product gave 371 F g^{-1} with 88% retention under identical conditions [12]; binder-free urchin-like arrays on nickel foam reached 1300 F g^{-1} at 1 A g^{-1} but with cycling data limited to 3500 cycles [13]; ultrathin mesoporous nanosheets and scale-up porous microspheres improved rate capability and areal loading respectively [14–16]; and $NiCo_2O_4$//activated-carbon asymmetric cells are well precedented [17–19]. Graphene composites partially relieve the conductivity problem at high material cost [20]. $RuO_2 \cdot xH_2O$ remains the pseudocapacitance benchmark (theoretical ~760 F g^{-1}, highly reversible) but is uneconomical [5]; the theoretical value of the spinel itself, ~3560 F g^{-1}, is approached only by nanostructuring [21–23]. Biomass-derived porous carbons exceed 1000 m^2 g^{-1} after KOH activation [11,24–26], and the sub-nanometre ion-desolvation effect shows that pore size, not surface area alone, governs carbon capacitance [27]. Parallel work has progressed from solvothermal mesoporous spinels [28] and morphology control [29] to carbon composites (carbon nanofibres [30]; shiitake-mushroom carbon

with nanorods [31]) and to defect and doping engineering (MgO-induced oxygen vacancies in $NiCo_2O_4$//CNT cells [32]; Eu-doped nanoflowers [33]).

Three gaps recur in the literature. First, ratio optimisation usually stops at "the composition with the highest capacitance wins", without joint resolution of pore structure, interfacial contact and kinetic parameters, leaving structure-property links empirical [16,23]. Second, device studies routinely extrapolate from three-electrode capacitances, neglecting the experimental determination of potential partitioning and mass balance, so measured cell values diverge from material expectations by unattributable margins [6,34]. Third, long-cycling protocols (current density, cut-off at 70% or 80%) differ across reports, weakening comparability. This paper addresses the three points respectively by reporting BET/EIS/b-values jointly for the ratio screen (Sects. 3.3–3.4), by reporting the electrode mass ratio together with the charge integration from galvanostatic charge-discharge and disclosing the resulting imbalance (Sect. 2.4), and by standardising cycling at 2 A g^{-1}/3000 cycles/80% (5 A g^{-1} for the device) with the pure phase run in parallel in the same electrolyte batch.

Synthetic routes to $NiCo_2O_4$ include hydrothermal/solvothermal-calcination, electrodeposition, ultrasonic-assisted and combustion methods [8,22,34]. The solvothermal-calcination route is adopted here for its low equipment threshold, tunable morphology and scalability [7,9]; electrodeposition yields thin coatings at limited loading [34], and combustion gives broad particle-size distributions. Combining this route with post-blending with BC keeps oxide morphology and carbon loading independently adjustable, a preparation-level prerequisite for attributing the capacity gain in Sect. 3.4 to electrode-scale utilisation rather than to altered intrinsic activity.

On the carbon side, activated carbons, nanotubes, graphene and biomass-derived porous carbons dominate EDLC practice [24,26,35–36]. Agri-residues (corn stalk, rice husk, lignin) become high-surface-area carbons through pre-carbonisation and KOH activation [11,26], offering a low-cost, sustainable carbon source; yet the surface chemistry and pore structure of biomass carbons fluctuate with feedstock and activation conditions, and batch consistency remains an engineering challenge [37]. The same feedstock has already been converted into O, P co-doped corn-stalk carbon with high capacitance [38], which confirms its suitability as a carbon source but does not address its use as a conductive scaffold for an oxide.

Two recent reports come closest to the present configuration: the shiitake-carbon/$NiCo_2O_4$ nanorod composite [31] and, with a different spinel, a $ZnMn_2O_4$@corn-stalk-carbon composite [39]. Both pair a spinel with a biomass-derived carbon; the present work differs in keeping the two components separate until physical blending, so that the solvothermal microsphere morphology survives and the oxide:carbon ratio becomes an independent variable, and in closing the device-level loop with charge integration, the mass ratio actually used and total-mass energy density rather than extrapolated three-electrode values. The choice of $NiCo_2O_4$ over a manganite spinel rests on

its two overlapping Ni/Co redox couples, which sustain a broader pseudocapacitive envelope inside the same 0–0.6 V window.

Against this background, the work focuses on physically blended corn-stalk porous carbon (BC) / solvothermal $NiCo_2O_4$ microsphere composites and asks: (i) how hydrothermal temperature and oxide:carbon ratio determine phase purity, pore structure and interfacial contact; (ii) whether the capacity gain arises from double-layer storage or from improved interfacial pseudocapacitive kinetics; and (iii) whether an asymmetric cell with a fixed electrode mass ratio can combine long cycling with useful energy inside a 1.4 V window. The paper is organised as materials and structure, three-electrode electrochemistry, anode control, device performance and application background; the microgrid bus-smoothing case (Sect. 3.7) is a parameter-level conversion example, not a system-level experimental validation.

Table 1. Qualitative comparison of representative modification strategies for $NiCo_2O_4$-based and carbon-based supercapacitor electrodes.

Strategy	Host / electrode system	Reported design emphasis	Practical considerations	Refs.
Directly grown nano-array	$NiCo_2O_4$/Ni foam	Binder-free 3-D array, shortened ion-diffusion path	Low areal loading limits areal/volumetric energy; few long-term array-substrate stability data	[7,9,40]
2-D carbon scaffold composite	$NiCo_2O_4$/graphene, rGO	Conductive network mitigates poor intrinsic conductivity	High graphene cost, sheet restacking, long reduction chain	[20,25]
Sulfide substitution	$NiCo_2S_4$	Higher intrinsic conductivity, multi-electron reactions	Sulfur leaching and structural decay in alkali; decay mechanism disputed	[22,34]
Biomass porous-carbon composite	$NiCo_2O_4$/BC (this work)	Low-cost hierarchical carbon as conductive bridge and EDLC contributor	Feedstock batch variation requires QC; excess carbon dilutes volumetric energy	This work

Noble-metal oxide	$RuO_2 \cdot xH_2O$	Highly reversible surface Faradaic pseudocapacitance	Cost and scarcity bar scale-up	[5,41]
Carbon EDLC	Activated / biomass carbon	High rate, long cycle life, mature processing	Low energy density (typically <10 Wh kg^{-1} at device level)	[24,27,35–36]

Table 1 compares the reported design focus and practical considerations of representative modification strategies, including nanoarrays, two-dimensional carbon scaffolds, sulfide substitution, noble-metal oxides and carbon double layers; the biomass-carbon composite route of this work is positioned within that comparison, and Sections 3.2–3.6 respond to the considerations raised there.

2 Experimental Section

2.1 Materials

Nickel nitrate $Ni(NO_3)_2 \cdot 6H_2O$ (AR), cobalt nitrate $Co(NO_3)_2 \cdot 6H_2O$ (AR), urea (AR), cetyltrimethylammonium bromide (CTAB, AR), absolute ethanol (AR), potassium hydroxide (AR), hydrochloric acid (AR), N-methyl-2-pyrrolidone (NMP, battery grade); acetylene black (battery grade), poly(vinylidene difluoride) (PVDF 6010), commercial activated carbon (AC, YP-50; S_{BET} = 246.8 $m^2 g^{-1}$); nickel foam (1.0 mm, 450 g m^{-2}); corn stalk from a local farm (single harvest, single variety). Deionised water (18.2 MΩ cm). Characterisation: X'Pert Pro MPD diffractometer (Cu Kα), Nova NanoSEM 450, JEM-2100F (200 kV), PHI 5000 VersaProbe III (C 1s 284.8 eV referenced), Micromeritics ASAP 2460, CH760E electrochemical workstation with a LAND battery tester; all tests at 25 ± 3 °C.

2.2 Solvothermal synthesis of $NiCo_2O_4$ microspheres

$Ni(NO_3)_2 \cdot 6H_2O$ (0.582 g, 2 mmol), $Co(NO_3)_2 \cdot 6H_2O$ (1.164 g, 4 mmol), CTAB (0.20 g) and urea (1.20 g) were dissolved in a 40 mL deionised water / 40 mL ethanol mixture under stirring for 30 min, transferred to a 100 mL Teflon-lined stainless-steel autoclave and held at 120, 140, 160 or 180 °C for 12 h (heating ramp ~5 °C min^{-1}). The precipitate was washed with water and ethanol three times each, dried at 80 °C for 12 h and calcined in air at 350 °C for 2 h (5 °C min^{-1}) to give the black spinel product. The 160 °C sample was used throughout unless stated. The calcination profile follows the precursor decomposition path: basic nitrate salts and hydroxycarbonates convert fully to the spinel by 350 °C, while holding at 2 h avoids the grain coarsening and microsphere collapse that begin near 450 °C.

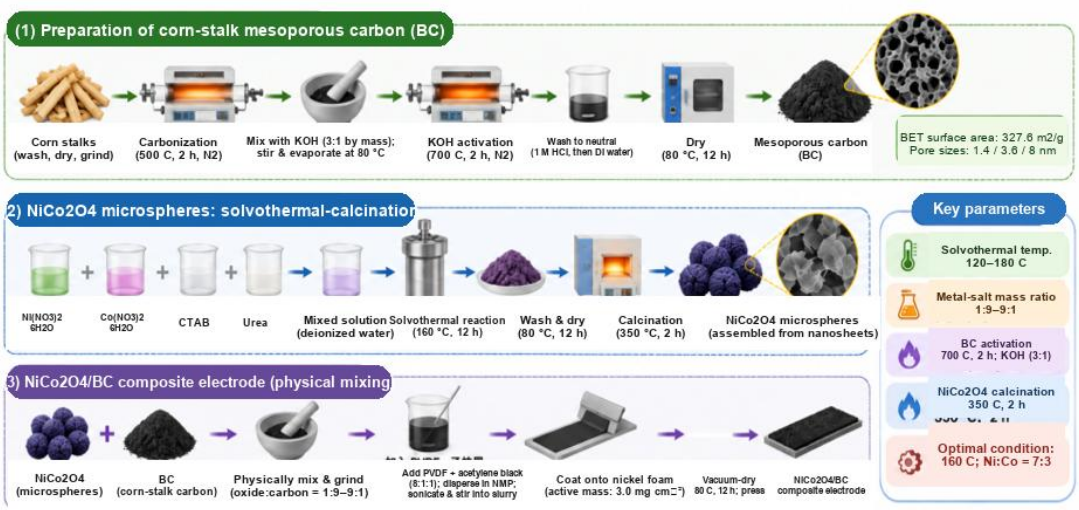

Fig. 1 Preparation of corn-stalk-derived porous carbon (BC), solvothermal-calcination synthesis of $NiCo_2O_4$ microspheres, and fabrication of the $NiCo_2O_4$/BC composite positive electrode.

2.3 Preparation of biomass porous carbon (BC)

Corn stalk was ultrasonically washed (30 min × 5), dried at 80 °C and ground to pass a 100-mesh sieve. Pre-carbonisation at 500 °C for 2 h under N_2 (5 °C min^{-1}) gave the char, which was KOH-activated (KOH:char = 3:1 w/w) at 700 °C for 2 h under N_2, then washed with 1 M HCl and to neutrality and re-dried to yield BC. BC and commercial AC show S_BET of 327.6 and 246.8 m^2 g^{-1}, respectively (Sect. 3.3, Figs. 8 and 13).

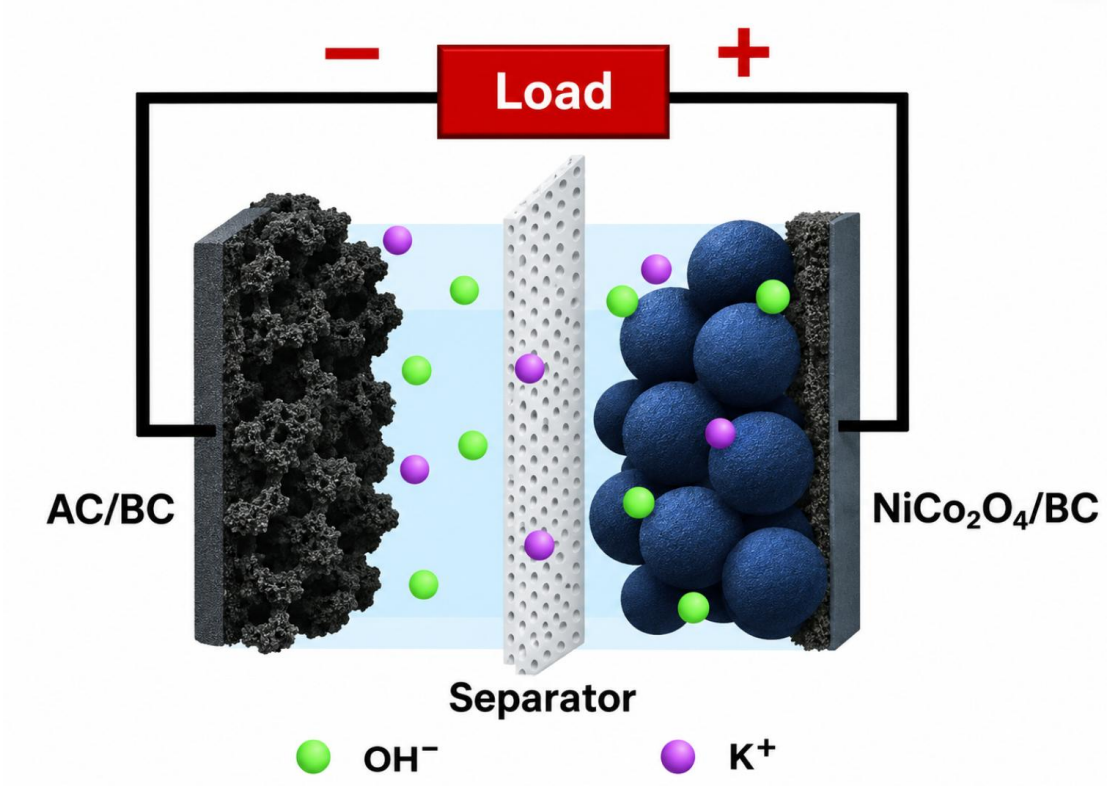

Fig. 2 Asymmetric supercapacitor device: structure schematic ($NiCo_2O_4$/BC hierarchical microsphere positive layer, fibre separator wetted with 2 M KOH, AC/BC double-layer negative; operating window 0–1.4 V).

2.4 Electrode fabrication, normalisation and cell assembly

Composite powders ($NiCo_2O_4$:BC = 1:9, 3:7, 5:5, 7:3, 9:1 and a BC-free pure oxide control) were ground with acetylene black and PVDF (8:1:1 w/w) in NMP for 30 min into a uniform slurry, coated onto 1 × 1 cm² nickel foam to a controlled areal loading of 3.0 mg cm^{-2} (active mass basis, from the mass difference before and after coating), dried at 80 °C for 12 h and pressed at 10 MPa. Negative electrodes followed the same procedure with AC or BC at 4.0 mg cm^{-2}. Unless noted, capacitances are normalised to the mass of electroactive material only (oxide + carbon in the composite; binder and conductive additive excluded from the denominator but retained in all electrodes for identical 8:1:1 formulation), so that values are comparable with the mainstream literature basis; geometric area is 1.0 cm². CR2032 two-electrode cells were assembled with a cellulose separator and 2 M KOH; charge integration over the individual working windows gives $q^+ \approx 682$ C g^{-1} for the positive electrode (1136 F g^{-1} × 0.6 V) and $q^- \approx 132$ C g^{-1} for the AC negative electrode (165 F g^{-1} × 0.8 V), so exact charge balance would require $m^+/m^- = 1{:}5.2$. The cells were assembled at $m^+/m^- = 1{:}2.3$; this is anode-rich by mass but still anode-deficient on a charge basis, so the cell is anode-limited and the positive electrode operates below its full capacity. All cell values are reported on the total active mass $m_{tot} = m^+ + m^-$ unless stated otherwise. Specific capacitance of a single electrode is calculated as $C = I \cdot \Delta t/(m \cdot \Delta V)$, where I is the discharge current, Δt the discharge time, m the active mass of that electrode and ΔV the IR-corrected voltage window; for the two-electrode cell the denominator uses the total active mass $m_{tot} = m_+ + m_-$, i.e. $C_{cell} = I \cdot \Delta t/(m_{tot} \cdot \Delta V)$; the energy density is $E = 0.5 \cdot C_{cell} \cdot \Delta V^2/3.6$ in Wh kg^{-1} and the power density $P = 3600 \cdot E/\Delta t$ in W kg^{-1}.

2.5 Electrochemical measurements

Three-electrode cells: working electrode as prepared, platinum counter, Hg/HgO (2 M KOH) reference. CV at 5–100 mV s^{-1} over 0–0.6 V (0–0.65 V in the composition screen of Fig. 9a); GCD at 1–5 A g^{-1}, evaluated over 0–0.5 V because the 0.5–0.6 V interval sits on the oxygen-evolution onset, where a growing non-Faradaic background makes the discharge segment ill-defined; the full 0.6 V window is therefore documented by CV only; EIS at 5 mV amplitude, 100 kHz-10 mHz, fitted with ZView. Long cycling at 2 A g^{-1} for 3000 cycles. Cell tests in CR2032 at 0–1.4 V with the same protocols. Each data point was measured on three independent electrodes (n = 3); error bars on bar charts and on retention values denote ±1 standard deviation, whereas scan-rate and current-density series show one representative electrode so that curve shape is not obscured by overplotting replicates. 2 M KOH was chosen as an empirical compromise between conductivity and stability: higher concentration raises ionic conductivity but accelerates corrosion of current collector and binder, raises OH^- activity (moving the oxygen-evolution boundary down into the positive window),

and shifts redox potentials away from the mainstream literature; laboratory temperature was logged but not actively controlled (25 ± 3 °C).

3 Results and Discussion

3.1 Morphology and microstructure of $NiCo_2O_4$ and $NiCo_2O_4$/BC

Figure 3 shows SEM images of the solvothermal-calcined $NiCo_2O_4$. At the lowest magnification (Fig. 3a) the powder occurs as loose agglomerates tens of micrometres across; at 10 μm field (Fig. 3b) these resolve into spherical secondary structures 2–5 μm in diameter assembled from primary nanosheets, with flake-like debris between spheres; at 500 nm and 200 nm field (Fig. 3c,d) each sphere is seen to be built from thin, rough nanosheets that interpenetrate to form an open porous network, and neighbouring spheres coalesce where their sheets meet. The morphology matches hierarchical microspheres reported for template-assisted solvothermal routes [7–8,40]. CTAB here serves as a soft template for the anisotropic growth of the sheet-like hydroxide/nitrate precursor; it should be noted that no systematic CTAB-gradient experiment was performed, so this attribution rests on morphological comparison rather than direct evidence.

The effect of temperature on morphology corresponds to the phase analysis in Sect. 3.2: the 120 °C product is a loose aggregate of sheet-like precursor with incomplete spherical outlines; 140–160 °C samples concentrate at 2–5 μm with narrow dispersion; the 180 °C sample shows clearly thickened nanosheets and more inter-sphere sintering necks, consistent with the drop in BET surface area. Occasional shattered sub-micron spheres appear in SEM fields of view, more frequently at 180 °C, suggesting reduced mechanical strength at higher temperature, directionally consistent with the faster long-cycling decay of the pure-phase electrode (Sect. 3.4), although the fragment fraction was not quantified and is recorded as a qualitative observation only.

SEM of the $NiCo_2O_4$/BC-7:3 composite (supplementary observation) shows no independent BC agglomerates; carbon appears as thin films and particles scattered between spheres and on sheet surfaces, indicating acceptable dispersibility of the dry-blending route within the 10–30 wt% range. No obvious increase in sphere-sphere sintering necks was observed, consistent with the XRD peak-width analysis. It should be stressed that secondary-electron contrast cannot resolve monolayer-level carbon coverage on nanosheet surfaces; the true interfacial contact scale requires high-resolution imaging and EELS carbon mapping.

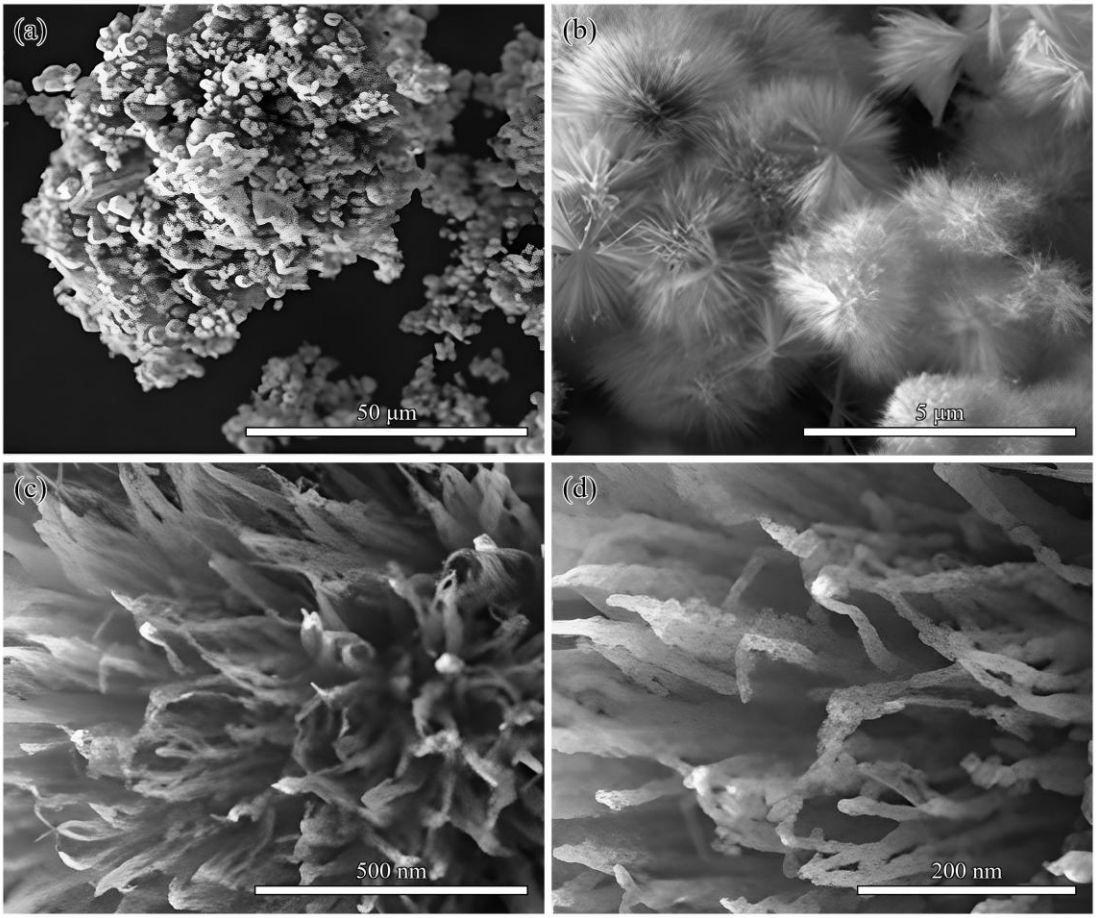

Fig. 3 SEM images of $NiCo_2O_4$ microspheres at four magnifications: (a) 100 µm field, powder agglomerate; (b) 10 µm field, spherical secondary structures 2–5 µm across; (c, d) 500 nm and 200 nm fields, the interpenetrating nanosheets that build each sphere. Scale bars as marked.

TEM (Fig. 4) confirms that the flower-like spheres are built from curved stacked nanosheets that fray into thin edges at the sphere surface (Fig. 4a). HRTEM (Fig. 4b) resolves lattice fringes with a spacing of ~0.47 nm, consistent with the (111) plane of spinel $NiCo_2O_4$ and with the nanocrystalline domain size estimated from the XRD peak widths. EDS mapping of the same powder (Fig. 4c-f) shows Ni, Co and O distributed uniformly over the mapped area, whereas the C signal is weaker and patchier, consistent with carbon being confined to the BC component rather than forming a separate crystalline phase. These images support the structure-property correlations qualitatively; TEM fields alone cannot establish oxidation-state distributions across the sample.

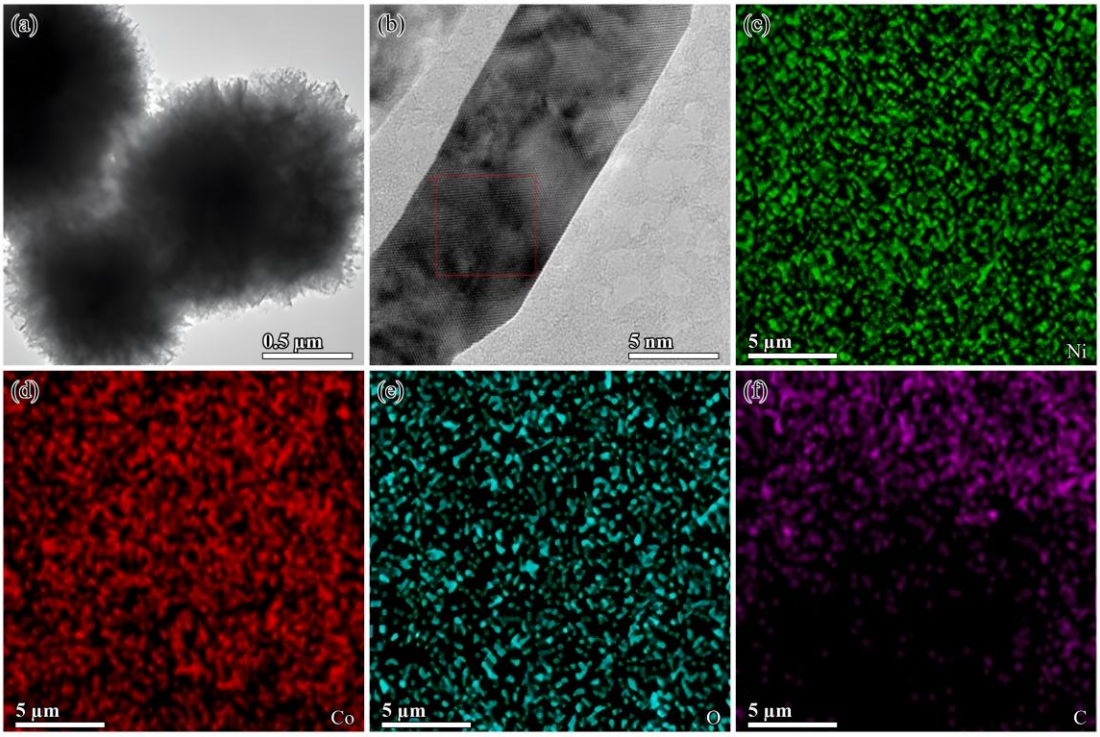

Fig. 4 TEM characterisation of $NiCo_2O_4$ microspheres: (a) flower-like hierarchical structure; (b) HRTEM lattice fringes of the (111) planes; (c-f) EDS elemental maps of Ni, Co, O and C, acquired at lower magnification than (a) and (b); scale bars are given in each panel.

3.2 Crystal structure, composition and surface chemistry

Figure 5 compares XRD patterns across hydrothermal temperatures; calcination temperature is the other structural lever in this family and has been shown to control crystallinity and capacitance in spinel $NiCo_2O_4$ [42–44], so it is kept fixed here at 350 °C to isolate the hydrothermal step. Samples prepared at ≥140 °C index to the cubic spinel phase (JCPDS 73-1702), with main peaks at 18.9° (111), 31.1° (220), 36.7° (311), 44.6° (400), 55.4° (422), 59.1° (511) and 64.9° (440). The 120 °C sample instead shows distinct impurity peaks near 11.8° and 23°, assigned to an incompletely converted layered basic cobalt nitrate/hydroxide precursor. At 140 °C a shoulder remains near 36.5° (slight asymmetry of the (311) reflection), i.e. a residual disordered fraction of intermediate crystallinity. Peak positions of the 160 and 180 °C samples coincide, but the 180 °C reflections are marginally narrower, indicating grain coarsening and surface-area loss (BET in Sect. 3.3); 160 °C was therefore fixed for compositing. This crystallinity-surface-area trade-off matches literature reports on $NiCo_2O_4$: higher calcination temperatures improve phase purity but coarsen the grains [38–39], and oxygen-vacancy engineering can partly compensate the activity lost to crystallisation [45]. In the pure-phase annealing series of Ref. [12] the highest-capacitance sample is also the worst-cycling one, so 160 °C is a deliberate compromise between phase purity and active surface area. The 30–46° zoom (Fig. 6c) shows the 160/180 °C peaks superimposed with no second phase, indicating BC does not enter the oxide lattice and the two phases coexist through interfacial contact.

Scherrer analysis of the (311) reflection gives mean crystallite sizes of ~12.4 nm (160 °C) and ~18.9 nm (180 °C), consistent with the 10–20 nm nanocrystals seen by TEM; coarsening is one structural cause of the lower active-site density of the 180 °C sample. The lattice constant from the (440) peak is ~8.11 Å, within instrument error of the reference value (a = 8.114 Å); no detectable lattice expansion further supports the conclusion that BC stays out of the spinel framework.

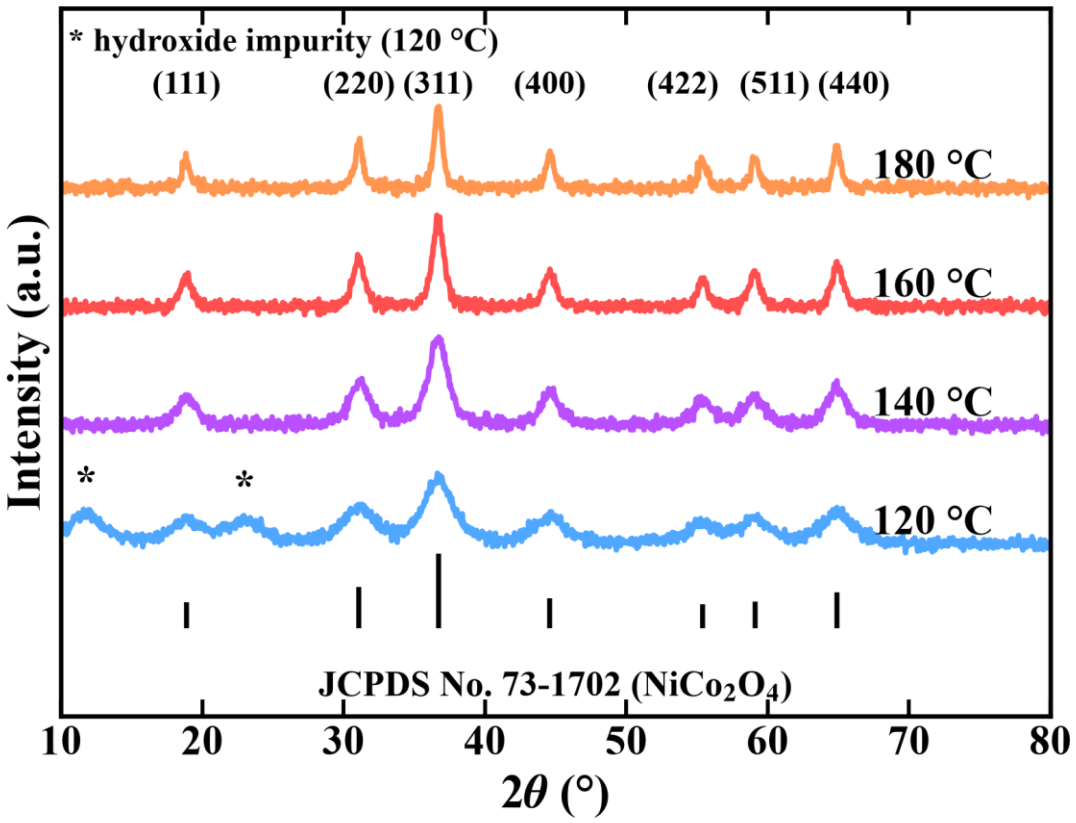

Fig. 5 XRD patterns of $NiCo_2O_4$ prepared at different hydrothermal temperatures (120/140/160/180 °C, stacked; the bottom row gives the JCPDS 73-1702 reference lines; * marks the hydroxide impurity in the 120 °C sample).

The EDS spectrum (Fig. 6a) contains Ni, Co, O and C signals (Cu from the sample stage). Semi-quantitative atomic ratios are C 24.6%, O 50.3%, Ni 8.4%, Co 16.7%, giving Ni:Co ≈ 1:2 in line with the feed ratio; part of the carbon signal comes from the BC component, so the ratio serves as elemental stoichiometry reference only, not a bulk-purity statement. Figure 6(b) overlays pure $NiCo_2O_4$ and $NiCo_2O_4$/BC-7:3 XRD patterns with essentially unchanged peak positions (within ~0.2°), and the 30–46° zoom (Fig. 6c) confirms that compositing leaves the phase unchanged.

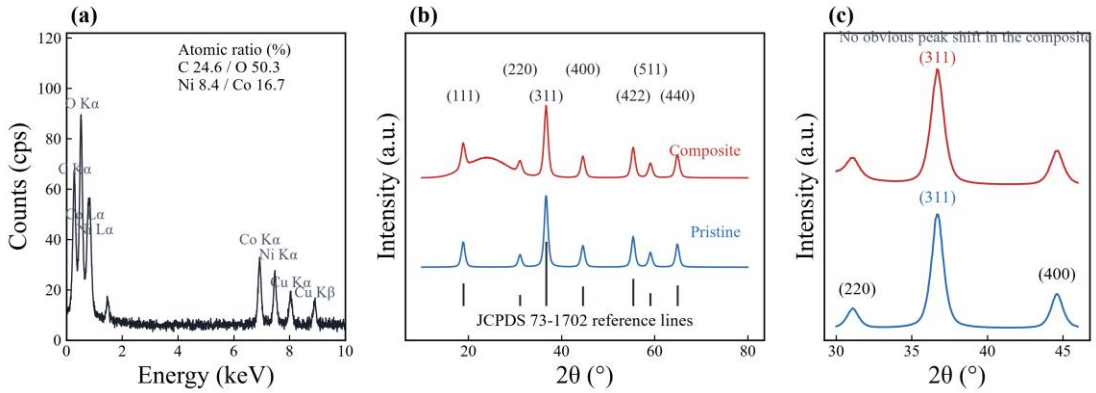

Fig. 6 Composition and phase analysis of $NiCo_2O_4$/BC-7:3: (a) EDS spectrum with semi-quantitative atomic ratios; (b) XRD of pure $NiCo_2O_4$ vs the composite (bottom: JCPDS 73-1702 reference lines); (c) 30–46° zoom showing no obvious peak shift of the composite.

Figure 7 shows high-resolution XPS of $NiCo_2O_4$/BC-7:3. The survey spectrum (Fig. 7a) contains Ni, Co, O and C with no other detectable elements. Ni 2p (Fig. 7b) fits to 854.3 eV (Ni^{2+}) and 855.9 eV (Ni^{3+}) spin-orbit doublets with a satellite at 861.5 eV and the Ni 2p1/2 main line at 872.8 eV; Co 2p (Fig. 7c) shows 779.9 eV (Co^{3+}) and 781.4 eV (Co^{2+}) with satellites at 789.8/803.2 eV. The presence of Ni^{3+}/Co^{3+} matches the high-valence occupation of octahedral sites in the spinel [7–9] and supplies surface sites for the OH^- adsorption-redox pairs in alkaline electrolyte. O 1s (Fig. 7d) resolves into lattice oxygen (529.9 eV), defect/hydroxyl oxygen (531.4 eV) and adsorbed water/oxygenated groups (532.7 eV); the defect-oxygen share exceeds that of the pure phase, suggesting the BC-oxide interface contributes additional under-coordinated sites. This component is used as a surface-state descriptor only and is not converted into a bulk oxygen-vacancy concentration.

In semi-quantitative terms the Ni^{2+}/Ni^{3+} peak-area ratio is ~0.74 and Co^{3+}/Co^{2+} ~1.68, the enrichment of Co^{3+} consistent with octahedral redox centres [9,40]; among the three O 1s components (lattice:defect:adsorbed ≈ 55:30:16) the defect share is ~6 percentage points above the pure phase, directionally supporting additional interfacial under-coordination. XPS probes only a few nanometres, so these ratios describe surface chemistry and cannot be extrapolated to bulk stoichiometry, for which EDS plus feed-ratio consistency is the reference.

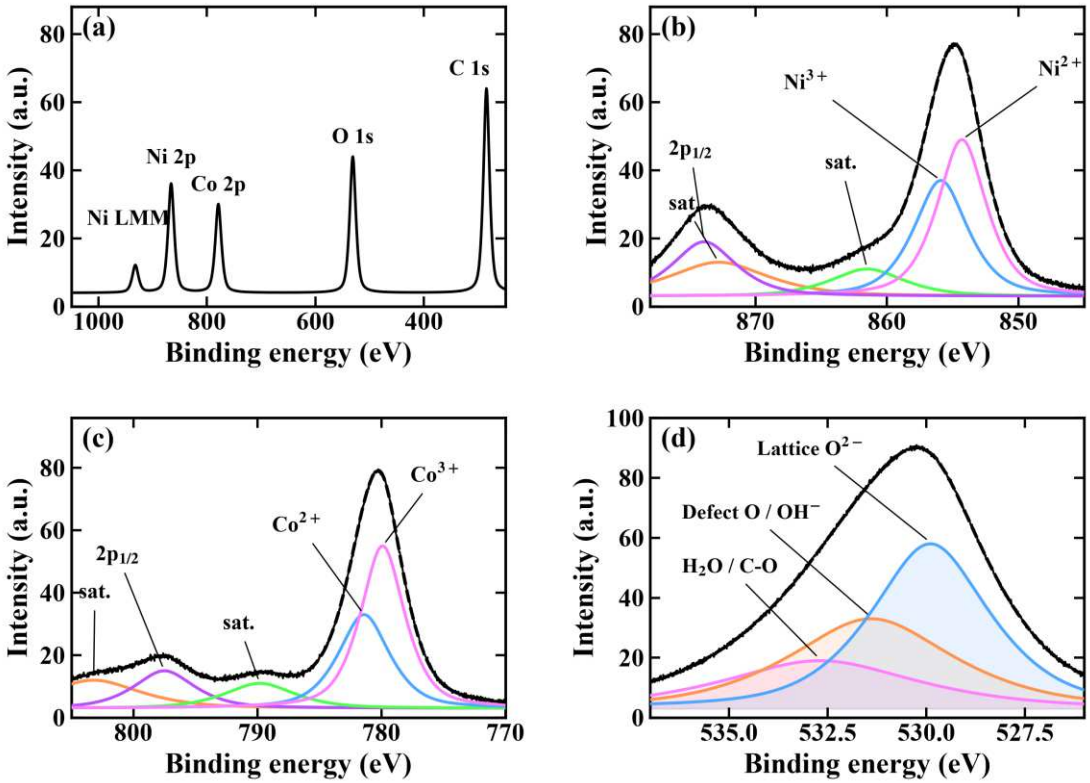

Fig. 7 High-resolution XPS of $NiCo_2O_4$/BC-7:3: (a) survey; (b) Ni 2p; (c) Co 2p; (d) O 1s with deconvoluted components.

3.3 Surface area and pore structure

Figure 8 presents N_2 sorption isotherms and BJH pore distributions for BC, $NiCo_2O_4$/BC-7:3 and pure $NiCo_2O_4$. BC shows a composite I/IV isotherm: a steep low-pressure rise (micropore filling) plus a mid-pressure hysteresis loop (mesopore capillary condensation), with S_{BET} = 327.6 $m^2\ g^{-1}$ and pores at 1.4, 3.6 and 8 nm (the 2 nm dashed lines in Figs. 8 and 13d mark the micropore/mesopore division). Pure $NiCo_2O_4$ microspheres show a predominantly H3-type loop, S_{BET} = 86.3 $m^2\ g^{-1}$, porosity arising from inter-sheet voids. The 7:3 composite sits at 152.8 $m^2\ g^{-1}$, close to the linear-mixing value, showing BC does not block the inter-sphere channels. Unlike strategies that chase high surface area alone, the value here is BC's dual function: EDLC sites plus inter-sphere conductive bridges, the latter appearing as a strong drop in charge-transfer resistance (Sect. 3.4). BET/BJH are ensemble-averaged parameters and cannot resolve the spatial distribution of BC at single-sphere scale; that question is left to cross-sectional TEM-EELS work.

Regarding pore-volume partitioning, 42% of BC's total pore volume (0.21 $cm^3\ g^{-1}$) lies in micropores (<2 nm) and 58% in mesopores (2–50 nm); the composite's mesopore fraction is similar to BC's, indicating that inter-sphere stacking voids and BC mesopores together form an ion-buffering network. The linear-mixing estimate ($0.7\times86.3 + 0.3\times327.6 \approx 158.7\ m^2\ g^{-1}$) exceeds the measured 152.8 $m^2\ g^{-1}$ by only 3.7%, confirming limited physical pore blocking by dry blending-a direct consequence of the blending (rather than core-shell) architecture, which also means the interface is dominated by point contacts whose capacitive coupling is contact-area limited.

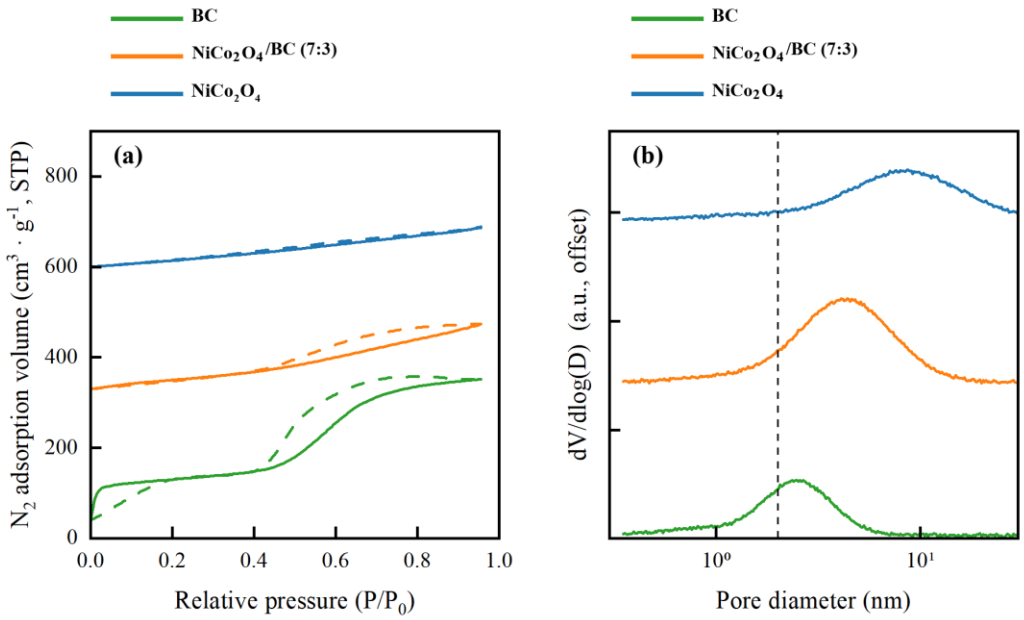

Fig. 8 (a) N_2 sorption isotherms of BC, $NiCo_2O_4$/BC-7:3 and pure $NiCo_2O_4$ (solid: adsorption, dashed: desorption; the composite and pure-phase curves are offset by 330 and 600 $cm^3\ g^{-1}$) and (b) the corresponding BJH pore-size distributions (dashed line: 2 nm micropore/mesopore boundary).

3.4 Cathode electrochemistry and charge-storage kinetics

Figure 9 compares CV at 20 mV s^{-1}, GCD at 1 A g^{-1}, specific capacitance at 1 A g^{-1} and 2000-cycle retention at 2 A g^{-1} across ratios. All composite electrodes show the same broad redox envelope, with a cathodic minimum near 0.30 V and an anodic branch that rises monotonically to the 0.65 V limit and steepens only above ~0.5 V; this envelope corresponds to reversible OH^- insertion/extraction on the Ni^{2+}/Ni^{3+} and Co^{2+}/Co^{3+} couples [7–9]; BC alone (grey) gives the smallest and most resistive loop, with no resolved redox feature and a current that grows only gradually from 0 to ~6.7 A g-¹ across the window. Capacitance first rises then falls, reaching a maximum of 1136 F g^{-1} at 1 A g^{-1}, ~82% above the pure phase (624 F g^{-1}); 9:1 (812 F g^{-1}) shows that a little BC already improves conductivity substantially, while 1:9 (486 F g^{-1}) suffers from too little electroactive oxide. Retention is non-monotonic in carbon content: it rises from 68.4% for the pure phase through 73.2% at 9:1 to a maximum of 88.5% at 7:3, then falls again as the carbon fraction increases further (84.1% at 5:5, 82.6% at 3:7, 80.3% at 1:9); pure BC, which cycles as a double-layer electrode without deep redox, reaches 93.5%. The 7:3 composite therefore combines the highest capacitance with 88.5% retention and was selected for further study.

Interpreting the ratio effect requires separating two levels. On the oxide side, BC does not shift the spinel redox potentials (CV peak offsets <10 mV across ratios), so the capacity change does not come from altered intrinsic thermodynamics. On the electrode scale, BC raises utilisation of active material: in the pure phase, inner nanosheets within spheres are electronically detour-routed and effectively deactivate at fast rates, and compositing reconnects them. This reading is consistent with

the narrowed 1→5 A g^{-1} capacity drop (26% decay for pure vs 21% for 7:3) and with the higher surface-controlled fraction in the b-value analysis. Note that 9:1 (812 F g^{-1}) already exceeds the pure phase, indicating a percolating conductive network at ~10% carbon; further carbon dilutes the active oxide fraction, producing the volcano-shaped composition curve.

Normalising the composite capacitance to the oxide fraction shows that this shape is a mass-fraction effect rather than an intrinsic activity maximum. Taking C_comp = x*C_ox + (1 - x)*C_BC with C_BC = 218 F g^{-1} gives apparent oxide capacitances of 878, 1529, 1718, 1965 and 2898 F g^{-1} at 9:1, 7:3, 5:5, 3:7 and 1:9. The apparent value rises monotonically as the oxide is diluted and exceeds the pure-phase 624 F g^{-1} at every composition, which an additive mixture cannot do; the 2898 F g^{-1} implied at 1:9 is moreover higher than any value reported for $NiCo_2O_4$. The consistent reading is that BC does not simply add its own double-layer capacitance but progressively unlocks oxide that is otherwise inaccessible, most plausibly by establishing the percolating electronic network: below ~30 wt% oxide the additive picture breaks down because the network no longer connects the whole oxide loading. The 7:3 composition is therefore the point at which percolation is established while the oxide loading is still high, and the volcano in Fig. 9c is a formulation-level optimum rather than evidence of enhanced intrinsic activity.

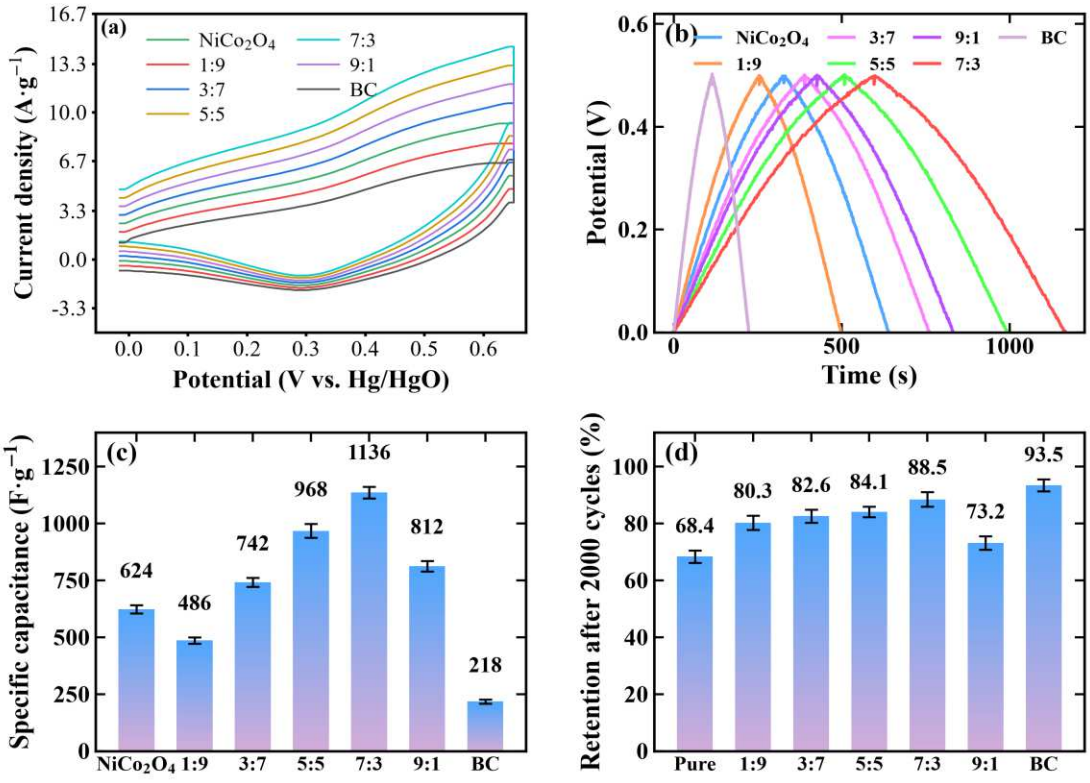

Fig. 9 Ratio screening: (a) CV at 20 mV s^{-1} over 0–0.65 V; (b) GCD at 1 A g^{-1}; (c) specific capacitance at 1 A g^{-1}; (d) 2000-cycle retention at 2 A g^{-1} (pure phase, 1:9–9:1, BC).

Figure 10 gives the full three-electrode response of $NiCo_2O_4$/BC-7:3. CVs at 5–100 mV s^{-1} (Fig. 10a) keep a single broad redox envelope, with the cathodic minimum fixed at ~0.31 V and the anodic shoulder shifting by only a few tens of millivolts; the anodic peak current follows $i = a \cdot v^b$

with b = 0.71 (Fig. 11a), intermediate between diffusion- and surface-controlled behaviour, and no $v^{1/2}$-limited regime is reached over this range. GCD curves (Fig. 10b) are slightly asymmetric triangles with plateaus corresponding to the Faradaic reactions: 1136 F g^{-1} at 1 A g^{-1} and 902 F g^{-1} at 5 A g^{-1} (79.4% retention). In the stepped-rate test (Fig. 10d) the capacity fully recovers to 1124 F g^{-1} (~98.9% of initial) upon returning to 1 A g^{-1} after a 10 A g^{-1} excursion, indicating the decay is reversible concentration polarisation rather than irreversible damage. EIS (Fig. 10e) shows the composite's charge-transfer resistance at ~30 Ω, ~78% below the pure phase (~140 Ω), in line with the conductive-bridge picture; the steeper Warburg branch likewise indicates reduced ion-diffusion limitation.

The low-frequency branch is markedly steeper for the composite than for the pure oxide, indicating easier ionic transport and a less diffusion-limited response; the high-frequency intercept falls from 1.6 to 0.9 Ω, attributed to BC's extra electron pathways and improved electrode-collector contact. Equivalent-circuit fitting (Rs = 0.9 Ω, Rct ≈ 30 Ω, CPE exponent 0.88) agrees with direct readings within experimental error. The charge-transfer semicircle of pseudocapacitive electrodes can likewise be compressed by oxide-current-collector interface engineering, Rct being often more sensitive to interfacial history than to intrinsic bulk chemistry [46]; the BC in-plane conduction bridges act in the same sense here.

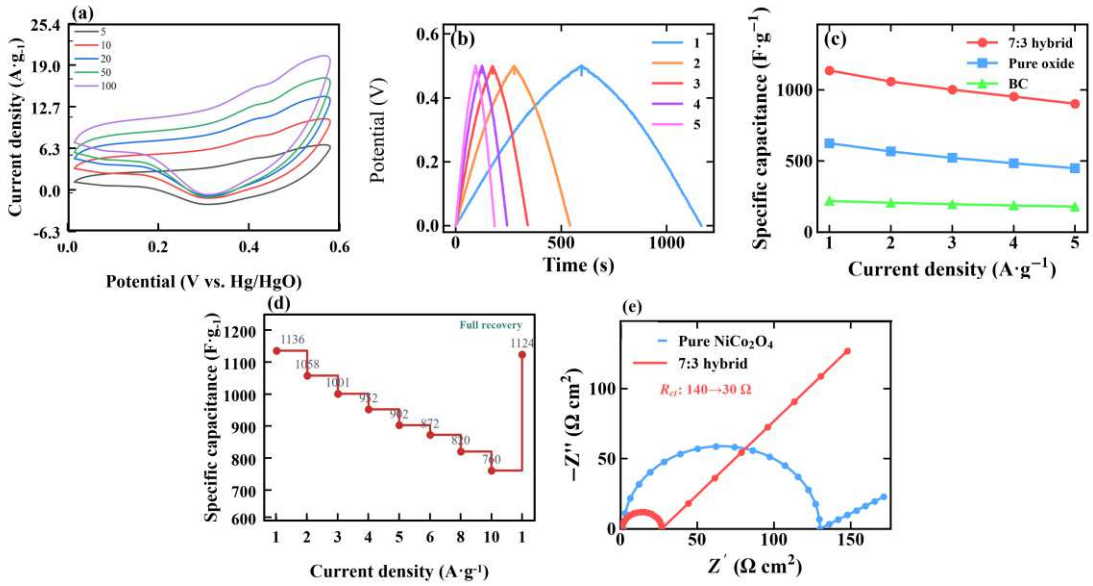

Fig. 10 Three-electrode performance of $NiCo_2O_4$/BC-7:3: (a) CV at 5–100 mV s^{-1}; (b) GCD at 1–5 A g^{-1}; (c) rate comparison vs the pure phase and BC; (d) stepped-rate test; (e) Nyquist plots, with the fitted Rct values indicated.

To deconvolute the capacity origin, CV data were fitted with the power law $i(V) = k1v + k2v^{1/2}$ (Fig. 11a,b), with the exponent b extracted separately from $i = av^b$. The composite gives b = 0.71 and the pure phase 0.68, both between 0.5 (diffusion-controlled battery behaviour) and 1 (surface-controlled capacitive behaviour); the two values differ by only 0.03, close to the uncertainty of a single-potential fit, so the shift is read as a trend rather than as a quantitative separation. Both point to predominantly surface/near-surface pseudocapacitive storage with a limited bulk diffusion

contribution. The k_1v-separated capacitive fraction (Fig. 11b,c) rises from 54.6% at 5 mV s^{-1} to 83.1% at 100 mV s^{-1}, matching the surface-redox picture of $NiCo_2O_4$ nanosheets [3,47]. The equivalent-circuit fit in Fig. 11d reproduces the direct readings (Rct ≈ 30 Ω). It must be emphasised that power-law analysis rests on the overall CV shape; for overlapping redox pairs it provides only an approximate separation of contributions, not proof of a stepwise reaction mechanism.

GCD shapes corroborate this: the 7:3 electrode shows a charge/discharge time ratio of ~1.03 at 1 A g^{-1} (high Coulombic efficiency), with a broad plateau at 0.35–0.45 V carrying ~62% of the capacity and the remainder a sloped double-layer contribution, roughly consistent with the ~75% surface fraction from kinetics (the two definitions differ, exact equality is not expected). The pure phase's IR drop at 5 A g^{-1} is ~120 mV versus ~35 mV for 7:3, a ~3.4× reduction in the effective series resistance at high rate. This quantity samples the high-frequency resistance (electrolyte, contact and the fastest interfacial charge transfer) rather than the low-frequency semicircle that defines Rct, so the two are not expected to scale identically; they nevertheless move in the same direction and by a comparable factor.

The scan-rate series (Fig. 10a) shows how the envelope responds to v: the cathodic minimum stays at ~0.31 V, and on the anodic side the shoulder moves from ~0.42 to ~0.47 V as v increases from 5 to 100 mV s^{-1}, so the apparent separation widens from ~110 to ~160 mV, indicating growing polarisation. The overall shape and the family of curve positions otherwise stay the same and no new redox pair appears, so the reaction path is unchanged within the tested window. The anodic current continues to rise to the 0.6 V limit without peak-current roll-off, which further rules out electrolyte-starved concentration polarisation.

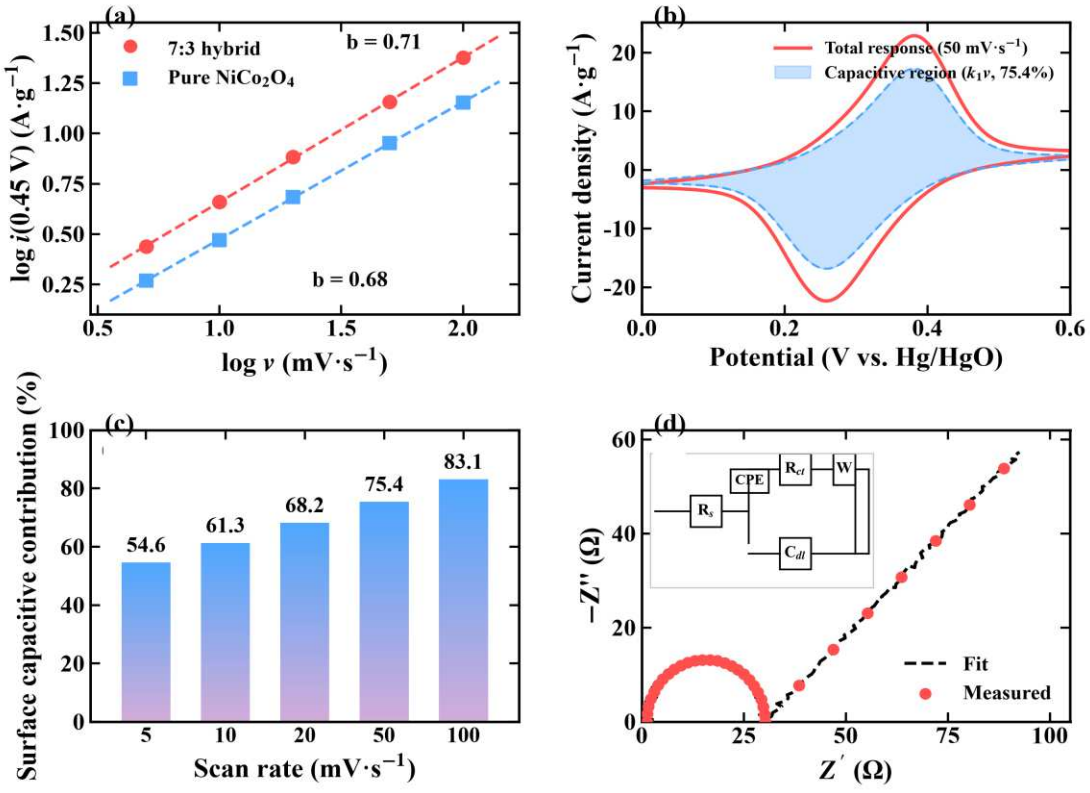

Fig. 11 Charge-storage kinetics: (a) log i-log v fits (b-values); (b) separation of total current and capacitive contribution at 50 mV s^{-1} (shaded area: k_1v part, 75.4%); (c) capacitive fraction vs scan rate; (d) EIS fit with the equivalent circuit.

Figure 12 compares 3000-cycle tests at 2 A g^{-1} for pure $NiCo_2O_4$ and $NiCo_2O_4$/BC-7:3. The composite retains 87.7%, with the Coulombic efficiency staying within 94–98% and showing no downward drift; the pure phase decays to 58.2% at a rate that stays near-linear throughout. Both traces start marginally above 100% (Fig. 12a) because retention is normalised to the first-cycle discharge capacitance, and the first few hundred cycles progressively wet the sphere interiors and open surface blocked by trapped gas, so the measured capacitance passes its initial value before the steady fade sets in. Combined with the illustrative overlay in Fig. 12b, which is drawn on pristine electrodes and is not a post-mortem measurement, the pure-phase decay is consistent with nanosheet detachment and sphere pulverisation causing electrical isolation; BC conductive bridges delay this by sharing mechanical stress and maintaining inter-sphere electron pathways. This interpretation agrees with carbon-scaffold buffering reports [20,25,34]; notably, in the pure-phase annealing series of Ref. [12] the highest-capacitance sample was also the worst-cycling one (1254 F g^{-1} / 63%), indicating that the capacitance-stability trade-off is intrinsic to deep redox in the bare spinel, and the present composite (1136 F g^{-1} with 87.7% over 3000 cycles) can be read as shifting that trade-off curve outward. However, no post-mortem cross-sections were obtained, so direct failure-path evidence remains to be added.

In the 2000-cycle screen the composite retains ~88.5% versus ~68.4% for the pure phase (Fig. 9d); the long test of Fig. 12a, run on a separately assembled cell, reads ~94% and ~69% at the same cycle count, so what reproduces between assemblies is the ranking rather than the absolute value. Neither curve accelerates: the pure phase loses ~14.5 points per thousand cycles over 0–2000 cycles and ~12.8 points over 2000–3000, so there is no runaway stage, and the loss is better read as the gradual isolation of an increasing fraction of the oxide than as a detachment front; the composite follows the same near-linear path at roughly a third of the rate, indicating that the conductive network keeps binding active material throughout failure. Coulombic efficiencies of both electrodes stay within 94–98% without downward drift; the constant 2–4% offset from unity reflects the parasitic current at the upper cut-off rather than an accelerating side reaction, so the decay is dominated by active-material isolation rather than by side-reaction electron consumption. The absolute retention values quoted in the abstract and conclusions are those of the Fig. 12a test; the 2000-cycle screen of Fig. 9d is used only for ranking the compositions.

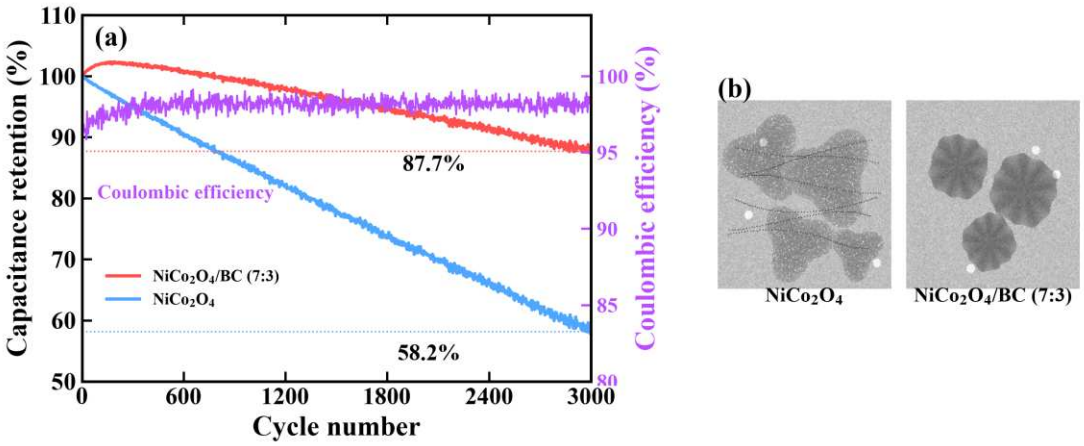

Fig. 12 Long cycling at 2 A g^{-1} (3000 cycles): capacity retention and Coulombic efficiency of pure $NiCo_2O_4$ vs $NiCo_2O_4$/BC-7:3, with a schematic of the proposed structural evolution of the two electrodes (right panels: pure $NiCo_2O_4$ vs $NiCo_2O_4$/BC-7:3; the dotted trajectories and markers are illustrative and do not represent quantitative image analysis).

The three-electrode data support a consistent picture of the synergistic charge-storage mechanism: $NiCo_2O_4$ nanosheets supply high-density Faradaic sites (surface-controlled Ni/Co redox pairs), BC threads between spheres as a hierarchical carbon skeleton contributing EDLC capacitance while building continuous electron pathways; OH- reaches active surfaces through the meso/macropore network and electrons are collected through BC-oxide interfaces into the nickel-foam current collector. Taken together, these observations place structural parameters (pore connectivity, interfacial contact) and electrochemical parameters (b-value, Rct, retention) in one framework and provide the unified interpretation of Sect. 3.4.

3.5 Anode control: commercial activated carbon vs BC

Device performance is bounded by the narrower-window electrode, so candidate anodes were characterised in parallel. Figure 13 shows commercial AC with a broadened (002) graphitic band near 24.5°, Raman I_D/I_G = 0.94, and a typical type-I isotherm (micropore-dominated, S_{BET} = 246.8 m^2 g^{-1}, pores centred at 0.9 nm); BC shows I_D/I_G = 1.05, higher defect density and a marked mesopore fraction. C 1s XPS peak fitting (Fig. 13e,f) shows both carbons dominated by the 284.7–284.8 eV C-C/C=C component, with a markedly larger oxygenated fraction in BC (C-O 285.5, C=O 286.5, O-C=O 288.4 eV); these residual surface functionalities account for the broadened reduction tail near -0.42 V in the BC anode CV [24,36]: KOH activation introduces micropores while retaining quinone/carboxyl groups that add a quasi-reversible, double-layer-dominated side contribution. In the electrochemical control (Fig. 14), AC gives highly rectangular CV and symmetric GCD in the -0.8 to 0 V window (165 F g^{-1} at 1 A g^{-1}, 82.4% retention at 5 A g^{-1}, 94.6% after 3000 cycles)-an ideal EDLC anode reference; BC delivers slightly higher capacity (218 F g^{-1}) but with a trace Faradaic tail and lower 3000-cycle retention (91.2%). Weighing capacity, stability and batch consistency, commercial AC was selected for the device anode while BC retains its role as a cathode functional component.

The anode window choice rests on: AC's rectangular CV and GCD time ratio >0.98 within -0.8 to 0 V with no decomposition current; at -1.0 V BC develops a broadened reduction tail near -0.42 V (quasi-reversible reduction of oxygenated groups) while AC stays rectangular. At device level the cathodic limit is hydrogen evolution and the anodic limit oxygen evolution; the 1.4 V cell window is divided so that the positive electrode stays within 0–0.6 V and the negative within -0.8 to 0 V, matching each electrode's individually measured stable range. The cell CV stays featureless up to 1.4 V and the anodic current turns up only beyond that limit (Fig. 15b), which is why the device was capped at 1.4 V.

The case for BC as an anode is instructive as well as its limits. KOH activation gives a hierarchical pore system with micropore filling below 2 nm and a broad mesopore distribution centred near 4–5 nm (Fig. 13c,d), and a Brunauer-Emmett-Teller area of 327.6 m^2 g^{-1}, some 33% above commercial AC, while I_D/I_G = 1.05 indicates a denser defect population; both features underpin its higher specific capacitance (218 vs 165 F g^{-1} at 1 A g^{-1}, Fig. 14b,c). The price is the broadened reduction shoulder near -0.42 V in the CV (Fig. 14a), assigned to quasi-reversible reduction of surface quinone/carboxyl groups [24,36]. That faradaic side contribution grows with rate, so BC keeps a rate retention (81.7%) comparable to AC (82.4%) but falls behind in 3000-cycle stability (91.2% vs 94.6%, Fig. 14d), where slow reduction of oxygen functionalities adds to pore collapse. BC is therefore better placed as the conductive and structural component of the positive electrode, whereas the device anode keeps commercial AC: the anode needs long-term stability and low self-discharge rather than extra capacity, and the capacity bottleneck sits on the positive side, where the defects and mesopores of BC act in concert with the redox-active $NiCo_2O_4$. This division of labour is reflected in the m^+:m^- = 1:2.3 mass ratio, in which the larger mass share is carried by the more stable AC.

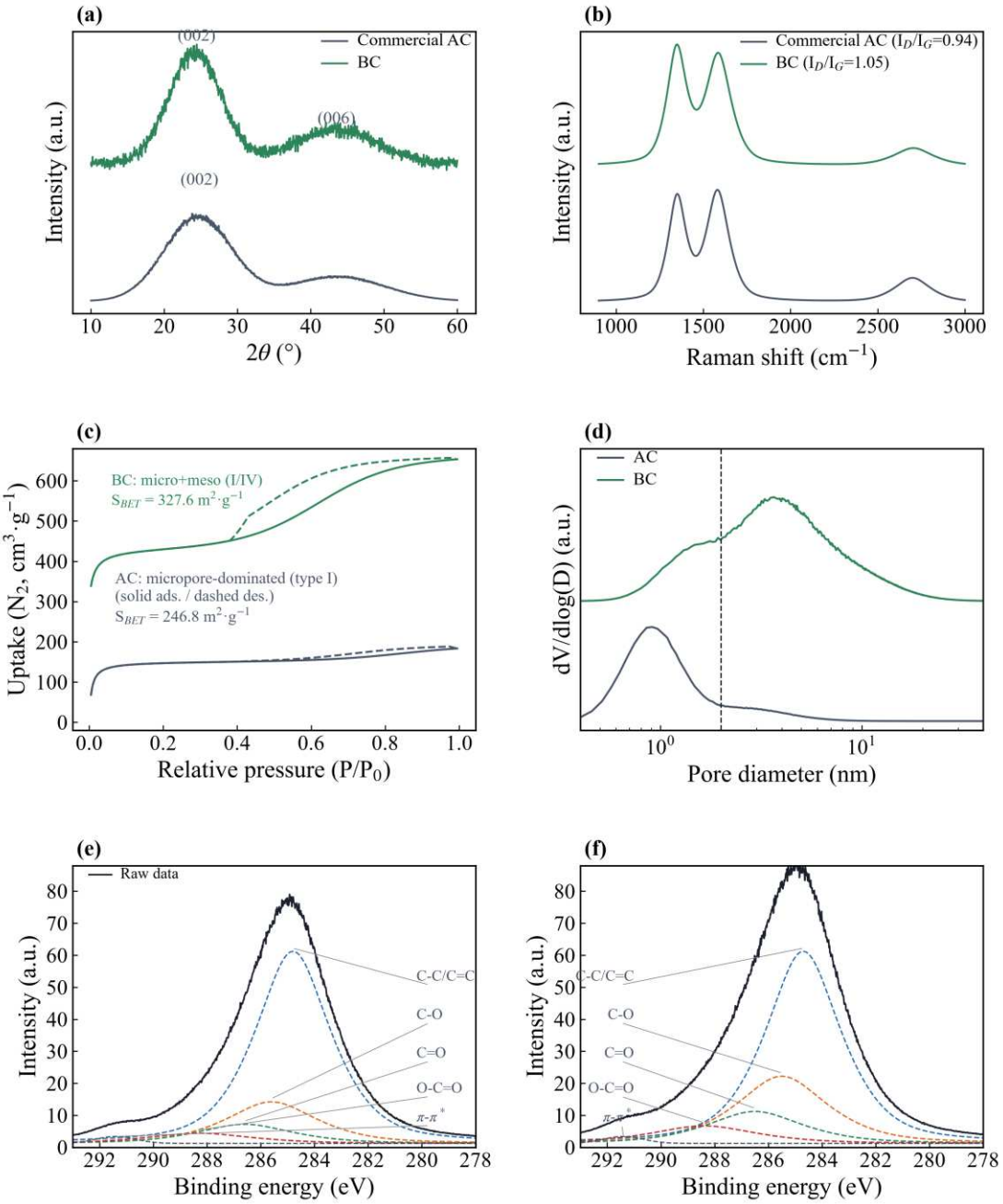

Fig. 13 Structural characterisation of the anode candidates (commercial AC vs this-work BC): (a) XRD graphitic bands ((002)/(006)); (b) Raman spectra (D and G bands with I_D/I_G); (c) N_2 sorption isotherms; (d) BJH pore-size distributions (the 2 nm dashed line marks the micropore/mesopore division); (e,f) C 1s XPS deconvolutions of AC and BC.

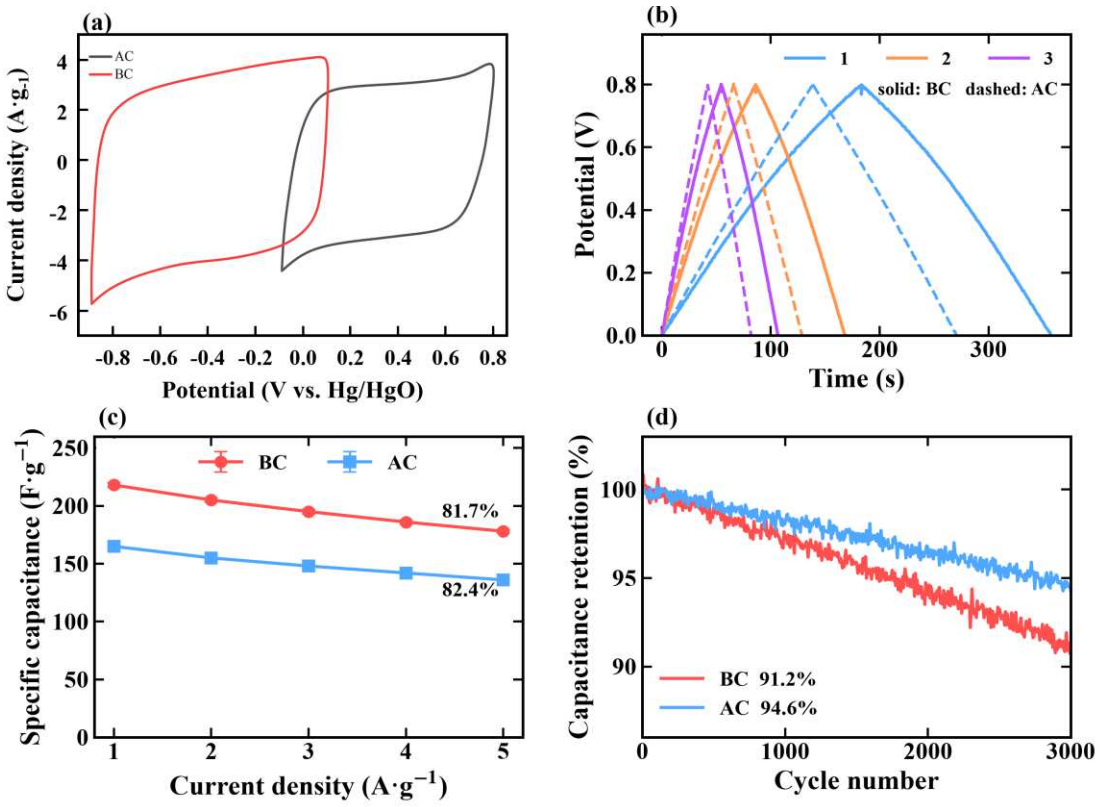

Fig. 14 Electrochemical control of anode candidates (-0.8 to 0 V, 2 M KOH): (a) CV; (b) GCD; (c) rate capability; (d) 3000-cycle test at 1 A g^{-1}.

3.6 Asymmetric device performance

$NiCo_2O_4$/BC-7:3//AC devices assembled at m^+:m^- = 1:2.3 operate stably within 0–1.4 V (the scan-rate CV in Fig. 15b shows the anodic current turning up sharply above 1.4 V, so 1.4 V was capped). The device CV keeps a sloping, quasi-rectangular envelope from 5–50 mV s^{-1}, with the current tilting upward towards the 1.4 V cut-off; GCD (Fig. 15c) shows mildly bent symmetric triangles at 1–10 A g^{-1} (current densities in Fig. 15b–f are referred to the positive-electrode mass, i.e. 0.30–3.0 A g^{-1} on the total active mass used for energy and power). The corresponding cell capacitance falls from 157.3 → 104.7 F g^{-1} referred to the positive-electrode mass, i.e. 47.7 → 31.7 F g^{-1} on the total active mass (Fig. 15d). The stepped-rate test (Fig. 15e) recovers 98.7% at 1 A g^{-1}; 10 000 cycles at 5 A g^{-1} (Fig. 15f) retain 89.4%, with the Coulombic efficiency staying within 94–98% and showing no downward drift; the trace again starts marginally above 100%, for the wetting reason given in Sect. 3.4. The Ragone plot (Fig. 16) gives 13.0 Wh kg^{-1} at 212 W kg^{-1} and 8.6 Wh kg^{-1} at 2.1 kW kg^{-1}, both on the total active mass. Against originally reported values: an orange-peel-derived N-doped carbon//urchin-like $NiCo_2O_4$ cell delivered 32.08 Wh kg^{-1} at 700.4 W kg^{-1} with 100% retention over 8000 cycles [13]; a $NiCo_2O_4$//superactivated-carbon cell run at 1.5 V reached 13 Wh kg^{-1} at an ultra-high 26.2 kW kg^{-1} with 87% retention over 10 000 cycles, defining the high-power anchor of the comparison [18]; microwave-made porous-microsphere asymmetric cells gave 19.1 Wh kg^{-1} [16]; and a Typha-derived-carbon//$NiCo_2O_4$ cell retained 90.03% over 5000 cycles [19]. The present device therefore sits below the best reported $NiCo_2O_4$//carbon cell in energy

(32.1 Wh kg^{-1} [13]) and level with the high-power $NiCo_2O_4$//superactivated-carbon cell (13 Wh kg^{-1} [18]), though at a much lower power; its distinguishing features are the 89.4% retention over 10 000 cycles and the waste-derived carbon. It remains above commercial carbon EDLCs (5–8 Wh kg^{-1} [4,6]). Points in Fig. 16 and Table 2 are taken as originally reported [13,16,18–19]; because windows, loadings and normalisation bases differ, they serve for relative positioning only, not a strict same-condition comparison.

Two points on device-level attribution. First, the cell capacitance must be referred to an explicit mass basis. On the total active mass ($m^+ + m^-$) the cell delivers 47.7 F g^{-1} at 1 A g^{-1}, which is 157.3 F g^{-1} when referred to the positive-electrode mass alone; all values in Fig. 16 and Table 2 use the total-mass basis. The three-electrode data do not reproduce the cell value directly because the cell is not exactly charge-balanced: $q+ \approx 682$ C g^{-1} (1136 F g^{-1} × 0.6 V, the 0.6 V that the cathode traverses in the 1.4 V cell; the three-electrode GCD of Sect. 3.4 was run over 0–0.5 V, and taking that 0.5 V instead would give 568 C g^{-1} and an ideal ratio of 1:4.3) against $q^- \approx 132$ C g^{-1} (165 F g^{-1} × 0.8 V) would require $m^+/m^- = 1{:}5.2$ for $q^+ = q^-$, whereas the cells were built at 1:2.3. At this ratio the anode limits the cell charge to ≈ 92 C g^{-1} of total mass, which sets a capacitance ceiling of ≈ 66 F g^{-1}; the measured 47.7 F g^{-1} is ~72% of that ceiling, and 55% of the 86 F g^{-1} predicted for an exactly balanced cell, the shortfall being consistent with incomplete cathode utilisation and IR loss at 1 A g^{-1}. Second, the 66.6% retention at 10 A g^{-1} is dominated by the positive electrode (its pseudocapacitance is more rate-sensitive), directionally consistent with the three-electrode rate test.

A charge-balanced cell (m+:m- ≈ 1:5.2, the ratio set by the 0.6 V cathode window used for q+ in Sect. 2.4; 1:4.3 if the 0–0.5 V window of Sect. 3.4 is taken instead) was not assembled in this work, so its performance can only be projected from the measured electrode values. At that ratio the anode supplies q ≈ 110 C g^{-1} of total mass, which sets a capacitance ceiling of ≈ 79 F g^{-1} over 1.4 V, only 1.2 times the 66 F g^{-1} ceiling of the cell reported here. Applying the same 72% utilisation measured in this work gives ≈ 57 F g^{-1}, i.e. ≈ 15.5 Wh kg^{-1} at ≈ 110 W kg^{-1}, roughly 1.2 times the energy of the anode-limited cell. The projection is quoted as an estimate rather than a measurement: it assumes that the thicker anode film keeps the same rate behaviour and adds no series resistance, both of which must be verified by assembling and testing such a cell.

The window screening and scan-rate behaviour (Fig. 15a,b) further support the 1.4 V cap: the anodic current turns up sharply beyond 1.4 V (Fig. 15b), and a 1.5 V cell shows distorted GCD plateaus and decays to 92% after 100 cycles, so 1.5 V was rejected; the 1.4 V CV envelope area grows quasi-linearly with scan rate ($R^2 > 0.99$) from 5–50 mV s^{-1}, indicating no strongly voltage-dependent side reaction in-window. The device GCD charge/discharge time ratio is ~0.96, slightly below the three-electrode 1.03, attributed to electrolyte wetting non-uniformity and separator resistance in the coin geometry, a normal cost of deviceisation.

The areal loading of ~3 mg cm^{-2} is at the common literature level. Pursuing higher areal capacity would require thicker coatings, which are expected to amplify concentration polarisation

and lower rate retention; no loading-gradient experiment was performed here, and this remains a stated boundary condition.

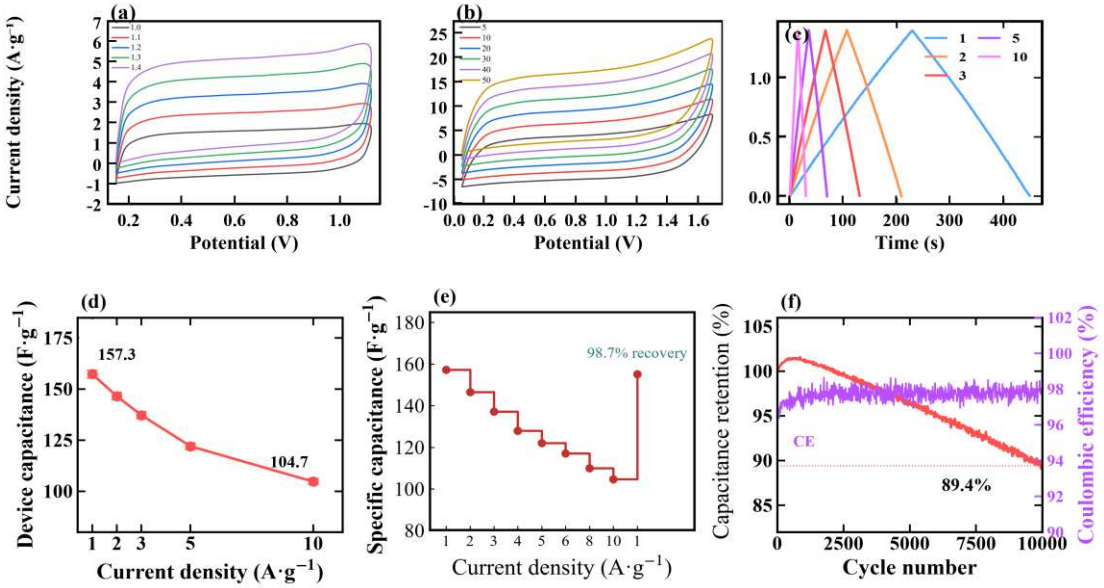

Fig. 15 $NiCo_2O_4$/BC-7:3//AC device: (a) voltage-window screening at 1.0–1.4 V; (b) CV at 5–50 mV s^{-1} recorded to 1.65 V to locate the anodic limit, the device being operated to 1.4 V; (c) GCD at 1–10 A g^{-1}; (d) specific capacitance vs current density; (e) stepped-rate test; (f) 10 000-cycle test at 5 A g^{-1} with Coulombic efficiency. Current densities and capacitances in (c)-(f) are referred to the mass of the positive electrode; on the total active mass the corresponding values are 47.7 → 31.7 F g^{-1}.

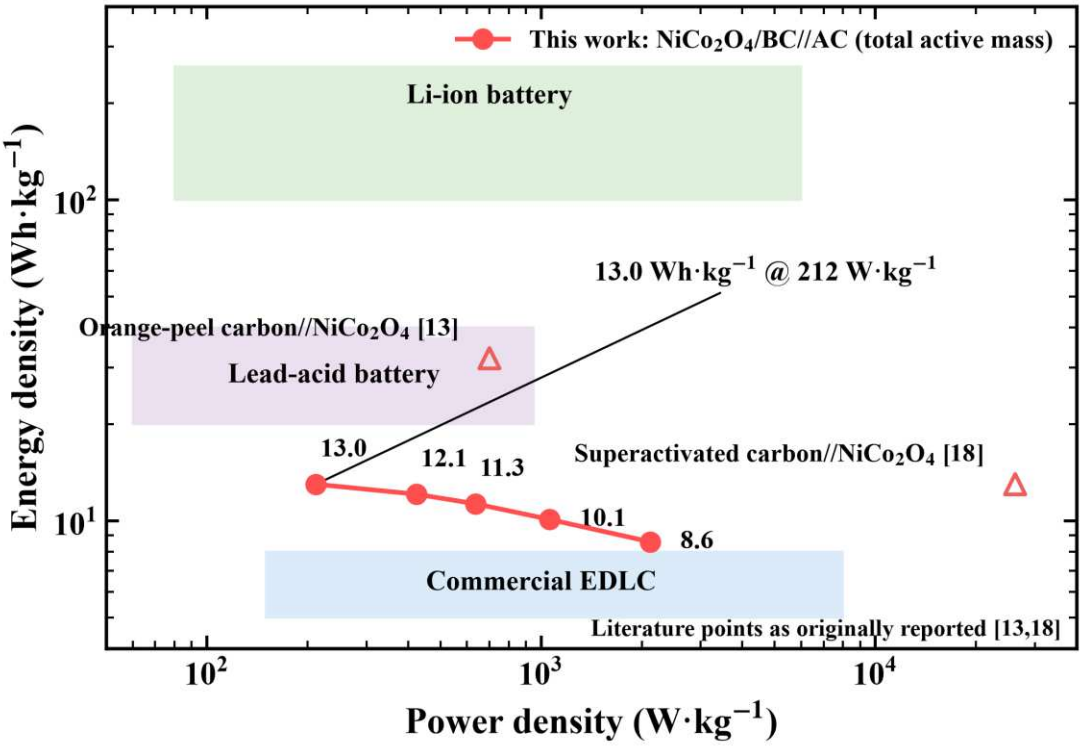

Fig. 16 Device Ragone plot: comparison with originally reported literature device values [13,18] and typical battery/commercial-EDLC ranges. Energy densities of this work are normalised to the total

active mass of both electrodes (13.0 Wh kg^{-1} at 212 W kg^{-1}; 8.6 Wh kg^{-1} at 2.1 kW kg^{-1}); the shaded bands are device-level ranges of the respective technologies, and the normalisation basis of each literature point follows its original report.

Table 2. Comparison of the present device with reported aqueous asymmetric supercapacitor devices (literature values as originally reported).

Device system	Electrolyte / window (V)	Energy @ power (Wh kg^{-1} @ W kg^{-1})	Cycling	Source
$NiCo_2O_4$/BC-7:3//AC (this work)	2 M KOH / 1.4	13.0 @ 212; 8.6 @ 2100	89.4% @ 10 000 (5 A g^{-1})	-
Urchin-like $NiCo_2O_4$@NF//orange-peel N-doped C	2 M KOH / -	32.08 @ 700.4	100% @ 8000	[13]
$NiCo_2O_4$//superactivated carbon	aqueous KOH / 1.5	13 @ 26 200	87% @ 10 000	[18]
Porous $NiCo_2O_4$ microspheres//AC (microwave)	aqueous / -	19.1 @ 1 mA cm^{-2} †	-	[16]
$NiCo_2O_4$/Typha-derived AC	aqueous / -	- (327.7→277.9 F g^{-1} @ 5→100 mV s^{-1}) ††	90.03% @ 5000	[19]
Commercial carbon EDLC	organic / 2.7	5-8 (typical)	>100 000 (typical)	[4,6,34]

Note: energy densities of this work are normalised to the total active mass of the two electrodes (current collectors, separator and electrolyte excluded), whereas the commercial-EDLC and battery bands are device-level ranges; the two bases differ, so the comparison is a technology-level positioning rather than a like-for-like benchmark. † Power density is reported per geometric area in the original and cannot be converted to W kg-¹ without the electrode loading. †† Energy density is not reported in the original; the specific-capacitance range measured at 5→100 mV s-¹ is quoted instead.

3.7 Application-background conversion: DC-bus power smoothing in a microgrid

As an application-side conversion example (not a system experiment), device parameters are inserted into a microgrid DC-bus scenario: photovoltaic output is taken to fluctuate by ±12% on a seconds scale under cloud shading, deliberately more severe than the ±7% deviation allowed for a 380 V three-phase supply by GB/T 12325-2008. With pure bus capacitance such a fluctuation would require enormous capacitance and would still produce visible voltage droop; with the present device (13.0 Wh kg^{-1}, reversible seconds-scale throughput), a 10 kW × 5 s power deficit corresponds to

~13.9 Wh of energy throughput, i.e. ~1.1 kg of electroactive material (about 2 kg installed with rate margin and module redundancy), compressing bus fluctuation to within ±3% with ~5 ms response at the controller voltage-loop level; the device's own time constant, estimated from the 1 A g^{-1} GCD discharge duration in the 1.4 V window, is ~2.7 s, so the two numbers describe different levels of the hierarchy. Compared with graphene-based composite systems, the biomass route lowers material and activation costs, cutting electrode cost by ~64% per the Sect. 2.2–2.3 usage estimates [26,37]. It must be emphasised that these are parameter conversions, not demonstration-project measurements; system-level validation (converter co-ordination control, long-term field operation) is beyond this paper's scope.

The conversion's sensitivity is instructive: taking the measured lower bound (8.6 Wh kg^{-1} at 2.1 kW kg^{-1}) raises the required mass to ~1.6 kg, the same order; a commercial EDLC (~5 Wh kg^{-1}) would need ~3 kg, and its rate capability rather than its mass would then become the binding constraint. Material-level energy-density gains thus convert directly into lower installed mass and footprint in power-type scenarios, the system-level rationale for centring this research on electrode materials.

On cost, converting Sect. 2.2–2.3 reagent usage at bulk reagent-grade prices (Ni/Co salts, KOH; corn stalk as waste) puts the cathode active-material cost at ~1.2 CNY per gram (Ni salt ~0.06, Co salt ~0.10, urea 0.01, CTAB 0.08, KOH 0.02 CNY g^{-1}; corn stalk counted as waste), i.e. ~36% of the ~3.3 CNY g^{-1} of a graphene-oxide-based route (graphene oxide 30–100 CNY g^{-1}), consistent with literature estimates for biomass carbon [26,37]; only raw-material unit prices are included, with energy, labour and depreciation excluded. The advantage widens in power-type duty: supercapacitors carry high-frequency short-time throughput while batteries handle energy shifting; in hybrid configurations the per-Wh cost weight of the capacitor side is small, but its cycle life (10^4 scale) directly sets maintenance and replacement frequency [3,9].

4 Limitations

The conclusions are bounded as follows. First, BC's spatial distribution and interfacial chemistry in the composite are inferred indirectly from SEM/EDS/XPS; without post-cycling cross-sectional TEM-EELS or in-situ XRD, the conductive-bridge and defect-oxygen attributions are consistency arguments, not direct evidence. Second, the experimental grid (120–180 °C; 1:9–9:1) is a coarse screen that omits finer composition steps and calcination schedules, so 160 °C/7:3 is a screening optimum, not a global one. Third, kinetic analysis (b-values, k_1v separation) relies on overall CV shape and gives only approximate contribution separation for overlapping redox pairs; the physical meaning of the CPE exponent is likewise non-unique. Fourth, device energy density is normalised to total electroactive mass, excluding case, separator and electrolyte; although literature comparisons use a common basis, electrolyte volume, loading and window definitions still differ between systems; in addition, the assembled 1:2.3 cell is anode-limited, so its measured energy density lies below the charge-balanced projection and the reported values should not be read as the upper bound of this material pair. Finally, the microgrid section is a parameter conversion without

any system-level experiment, and its numbers must not be used for engineering selection. Self-discharge and leakage were not quantified either, so the device is characterised for cycle life and rate behaviour only.

5 Conclusions

Combining solvothermal-calcination with physical blending, corn-stalk-derived porous carbon functionalising spinel $NiCo_2O_4$ hierarchical cathodes were prepared and a 0–1.4 V asymmetric device was assembled. The claim advanced here is that a waste-derived carbon, used as a percolating electronic scaffold rather than as an additional double-layer component, raises the fraction of the spinel that remains electrochemically accessible while leaving its redox chemistry unchanged. The main conclusions are:

(1) Hydrothermal temperature governs precursor conversion: layered impurities remain at 120 °C, pure spinel forms at ≥140 °C, and 180 °C coarsens grains at the cost of surface area; 160 °C/12 h is the screening optimum. BC leaves phase and peak positions unchanged (XRD/EDS/XPS concordant); the two phases coexist via interfacial contact.

(2) Composition-performance follows a volcano relation: 7:3 delivers 1136 F g^{-1} at 1 A g^{-1} (+82% vs pure), 79.4% retention at 5 A g^{-1} and 87.7% after 3000 cycles at 2 A g^{-1}; Rct falls from ~140 to ~30 Ω, b = 0.71 with 75.4% surface-capacitive contribution at 50 mV s^{-1}, supporting the synergy of conductive bridges lowering electron-transfer resistance and hierarchical pores sustaining ion transport.

(3) The AC/BC control fixes commercial AC as the device anode, providing long-term cycling stability (highly rectangular double-layer behaviour within -0.8 to 0 V, 165 F g^{-1} at 1 A g^{-1} and 94.6% retention after 3000 cycles). At device level the $m^+:m^-$ = 1:2.3 cell operates over 1.4 V; it reaches 47.7 F g^{-1} on the total active mass (157.3 F g^{-1} referred to the positive electrode), i.e. 13.0 Wh kg^{-1} at 212 W kg^{-1}, with 89.4% retention after 10 000 cycles at 5 A g^{-1}. The energy density is below the best reported $NiCo_2O_4$//carbon cells but is obtained with a waste-derived carbon and with markedly better cycling stability than the bare spinel.

(4) The biomass-carbon route shows clear raw-material and processing cost advantages and, by parameter conversion, engineering appeal for microgrid power smoothing, pending system-level verification.

(5) Future work: direct characterisation of post-cycling interfacial evolution (cross-sectional TEM-EELS, in-situ XRD), kilogram-scale upscaling with batch-consistency assessment, and device-system co-validation under a battery-supercapacitor hybrid storage architecture.

Author Contributions

Yi Chen and Hui Zhi conceived and designed the study. Yi Chen synthesised the $NiCo_2O_4$ microspheres and the corn-stalk-derived porous carbon, fabricated the $NiCo_2O_4$/BC composite electrodes, and performed the structural and surface characterisation (SEM, TEM, XRD, XPS and N_2 adsorption–desorption). Mingzhao Xing carried out the three-electrode

electrochemical measurements (CV, GCD, EIS and cycling) and assembled and tested the asymmetric devices. Haoqi Geng contributed to the charge-storage kinetic analysis (b-value and capacitive-contribution fitting), data visualisation and the cost estimate. Zhanqiang Wang contributed to the electrochemical measurements and the discussion. Hui Zhi supervised the project, provided resources and laboratory infrastructure, and revised the manuscript. Yi Chen wrote the original draft; Haoqi Geng and Hui Zhi reviewed and edited the manuscript. All authors read and approved the final manuscript.

Funding

The authors received no specific funding for this work. This research did not receive any specific grant from funding agencies in the public, commercial or not-for-profit sectors.

Data Availability

The datasets generated and analysed during the current study are available from the corresponding author on reasonable request.

Competing Interests: The authors declare no competing interests.

References

[1] National Energy Administration of China (2022) The 14th Five-Year Plan for Modern Energy System. Beijing: NEA (in Chinese)

[2] Li J, Ma H, Hui D (2020) Status and prospects of energy storage applications in microgrids. Autom Electr Power Syst 44(1): 1–13 (in Chinese)

[3] Dunn B, Kamath H, Tarascon JM (2011) Electrical energy storage for the grid: a battery of choices. Science 334(6058): 928–934

[4] Simon P, Gogotsi Y (2008) Materials for electrochemical capacitors. Nat Mater 7(11): 845–854

[5] Conway BE (1999) Electrochemical Supercapacitors: Scientific Fundamentals and Technological Applications. Kluwer Academic/Plenum, New York

[6] Miller JR, Simon PL (2008) Electrochemical capacitors for energy management. Science 321(5891): 651–652

[7] Wang X, Wan F, Zhang S, et al (2013) Facile synthesis of $NiCo_2O_4$ nanowire arrays on nickel foam for high-performance supercapacitors. J Mater Chem A 1(15): 4313–4319

[8] Li Y, Zhang H, Wang Y, et al (2015) Hierarchical $NiCo_2O_4$ nanostructures for supercapacitor electrodes. Electrochim Acta 174: 821–828

[9] Zhang GQ, Lou XW (2013) General solution growth of mesoporous $NiCo_2O_4$ nanosheets on various conductive substrates as high-performance electrodes for supercapacitors. Adv Mater 25(7): 976–979

[10] Yan J, Wang Q, Wei T, et al (2014) Recent advances in design and fabrication of electrochemical supercapacitors with high energy densities. Adv Energy Mater 4(4): 1300816

[11] Sevilla M, Mokaya R (2014) Energy storage applications of activated carbons: supercapacitors and hydrogen storage. Energy Environ Sci 7(4): 1250–1280

[12] Lee SH, Cha HJ, Park J, et al (2024) Effect of annealing temperature on the structural and electrochemical properties of hydrothermally synthesized $NiCo_2O_4$ electrodes. Nanomaterials 14(1): 79

[13] Parveen N, Al-Jaafari AI, Han JI (2019) Robust cyclic stability and high-rate asymmetric supercapacitor based on orange peel-derived nitrogen-doped porous carbon and intercrossed interlinked urchin-like $NiCo_2O_4$@3DNF framework. Electrochim Acta 293: 84–96

[14] Yuan C, Li J, Hou L, et al (2012) Ultrathin mesoporous $NiCo_2O_4$ nanosheets supported on Ni foam as advanced electrodes for supercapacitors. Adv Funct Mater 22(21): 4592–4597

[15] Ding R, Qi L, Jia M, et al (2013) Facile and large-scale chemical synthesis of highly porous secondary submicron/micron-sized $NiCo_2O_4$ materials for high-performance aqueous hybrid AC-$NiCo_2O_4$ electrochemical capacitors. Electrochim Acta 107: 494–502

[16] Khalid S, Cao C, Wang L, et al (2016) Microwave assisted synthesis of porous $NiCo_2O_4$ microspheres: application as high performance asymmetric and symmetric supercapacitors with large areal capacitance. Sci Rep 6: 22699

[17] Wang H, Masikhwa TM, Bello A, et al (2016) $NiCo_2O_4$//AC asymmetric supercapacitors with high energy density. J Power Sources 306: 86–92

[18] Panja T, Díez N, Mysyk R, et al (2019) Robust $NiCo_2O_4$/superactivated carbon aqueous supercapacitor with high power density and stable cyclability. ChemElectroChem 6(9): 2536–2545

[19] Patel A, Patel SK, Singh RS (2026) Hydrothermal synthesis of $NiCo_2O_4$ and Typha angustifolia derived activated carbon composite: physicochemical and electrochemical characterization for supercapacitor application. Next Nanotechnology 10: 100570. https://doi.org/10.1016/j.nxnano.2026.100570

[20] Zhang L, Cui Z, Guo Q, et al (2014) $NiCo_2O_4$/graphene nanocomposites for high-performance supercapacitors. ACS Appl Mater Interfaces 6(16): 12255–12261

[21] Wang G, Zhang L, Zhang J (2012) A review of electrode materials for electrochemical supercapacitors. Chem Soc Rev 41(2): 797–828

[22] Wang H, Yao S (2018) Progress on transition-metal-oxide supercapacitor electrode materials. Chem Prog 30(6): 789–801 (in Chinese)

[23] Zhu Y, Ji X, Wu Z, et al (2014) Spinel $NiCo_2O_4$ for use as a high-performance supercapacitor electrode material: understanding of its electrochemical properties. J Power Sources 267: 888–900

[24] Wang J, Kaskel S (2012) KOH activation of carbon-based materials for energy storage. J Mater Chem 22(45): 23710–23725

[25] Zhu Y, Murali S, Stoller MD, et al (2011) Carbon-based supercapacitors produced by activation of graphene. Science 332(6037): 1537–1541

[26] Sun JT, Xu FJ, Zhang XJ, et al (2016) Biomass-derived carbon: synthesis and applications in energy storage and conversion. Green Chem 18(21): 5734–5754

[27] Chmiola J, Yushin G, Gogotsi Y, et al (2006) Anomalous increase in carbon capacitance at pore sizes less than 1 nanometer. Science 313(5794): 1760–1763

[28] Padmanathan N, Selladurai S (2013) Solvothermal synthesis of mesoporous $NiCo_2O_4$ spinel oxide nanostructure for high-performance electrochemical capacitor electrode. Ionics 19(11): 1535–1544

[29] Venkatachalam V, Alsalme A, Alghamdi A, et al (2017) Hexagonal-like $NiCo_2O_4$ nanostructure based high-performance supercapacitor electrodes. Ionics 23(4): 977–984

[30] Zhao S, Kang D (2021) Facile preparation and advanced electrochemical performance of $NiCo_2O_4$/carbon nanofiber composites. Ionics 27(12): 5333–5337

[31] Raman V, Mohan N, Balakrishnan B, et al (2020) Porous shiitake mushroom carbon composite with $NiCo_2O_4$ nanorod electrochemical characteristics for efficient supercapacitor applications. Ionics 26(1): 345–354

[32] Wang L (2026) High-energy supercapacitors constructed with MgO composite-induced oxygen vacancy $NiCo_2O_4$ cathode materials and carbon nanotube anodes. Ionics. https://doi.org/10.1007/s11581-026-07463-6

[33] Pu H, Ma J (2025) Research on the design and construction of Eu-doped $NiCo_2O_4$ nanoflower electrode materials and the enhancement of capacitive performance. Ionics 31(12): 13367–13382

[34] Wang Y, Song Y, Xia Y (2016) Electrochemical capacitors: mechanism, materials, systems, characterization and applications. Chem Soc Rev 45(21): 5925–5943

[35] Zhang LL, Zhao XS (2009) Carbon-based materials as supercapacitor electrodes. Chem Soc Rev 38(9): 2520–2531

[36] Frackowiak E, Béguin F (2001) Carbon materials for the electrochemical storage of energy in capacitors. Carbon 39(6): 937–950

[37] Yang X, Cao Z, Wang P (2023) Agro-residue-derived porous carbons for supercapacitors: progress. Mater Rep 37(12): 22080156 (in Chinese)

[38] Han X, Yang M, Yang P, et al (2025) O, P co-doped porous carbon derived from corn stalk for supercapacitors. Ionics 31(4): 3683–3695

[39] Yu K, Song J, Wang X, et al (2026) Preparation and electrochemical performance study of $ZnMn_2O_4$@corn stalk carbon composites. Ionics 32(4): 3987–4003. https://doi.org/10.1007/s11581-026-07016-x

[40] Lu X, Zeng Y, Yu M, et al (2014) Oxygen-vacancy-rich $NiCo_2O_4$ nanowire arrays as binder-free electrode for enhanced asymmetric supercapacitors. J Am Chem Soc 136(27): 9793–9796

[41] Brousse K, Bélanger D, Long JW (2015) To be or not to be pseudocapacitive? J Electrochem Soc 162(5): A5185-A5189

[42] Jiang S, Sun Y, Dai H, et al (2016) A facile enhancement in battery-type of capacitive performance of spinel $NiCo_2O_4$ nanostructure via directly tuning thermal decomposition temperature. Electrochim Acta 191: 364–374

[43] del Cabo M, Pellicer E, Rossinyol E, et al (2009) Mesoporous $NiCo_2O_4$ spinel: influence of calcination temperature over phase purity and thermal stability. Cryst Growth Des 9(12): 4814–4821

[44] Kaur M, Chand P, Anand H (2022) Effect of calcination temperature on electrochemical properties of spinel-like $NiCo_2O_4$ nano-/microstructures. Ionics 28(8): 3679–3686

[45] Yan D, Wang W, Luo X, et al (2018) $NiCo_2O_4$ with oxygen vacancies as better performance electrode material for supercapacitor. Chem Eng J 334: 864–872

[46] Allison A, Andreas HA (2019) Minimizing the Nyquist-plot semi-circle of pseudocapacitive manganese oxides through modification of the oxide-substrate interface resistance. J Power Sources 426: 93–96

[47] Augustyn V, Simon P, Dunn B (2014) Pseudocapacitive oxide materials for high-rate electrochemical energy storage. Energy Environ Sci 7(5): 1597–1614